AFRL-AFOSR-VA-TR-2018-0362

Multisensory integration for adaptive flight control

Susanne Sterbing-D'Angelo
MARYLAND UNIV COLLEGE PARK
3112 LEE BLDG
COLLEGE PARK, MD 20742 - 5100

10/03/2018
Final Report

REPORT DOCUMENTATION PAGE

Form Approved
OMB No. 0704-0188

The public reporting burden for this collection of information is estimated to average 1 hour per response, including the time for reviewing instructions, searching existing data sources, gathering and maintaining the data needed, and completing and reviewing the collection of information. Send comments regarding this burden estimate or any other aspect of this collection of information, including suggestions for reducing the burden, to Department of Defense, Executive Services, Directorate (0704-0188). Respondents should be aware that notwithstanding any other provision of law, no person shall be subject to any penalty for failing to comply with a collection of information if it does not display a currently valid OMB control number.
PLEASE DO NOT RETURN YOUR FORM TO THE ABOVE ORGANIZATION.

1. REPORT DATE *(DD-MM-YYYY)*	2. REPORT TYPE	3. DATES COVERED *(From - To)*
03-10-2018	Final Performance	01 Apr 2012 to 30 Sep 2017

4. TITLE AND SUBTITLE
Multisensory integration for adaptive flight control

5a. CONTRACT NUMBER

5b. GRANT NUMBER
FA9550-12-1-0109

5c. PROGRAM ELEMENT NUMBER
61102F

6. AUTHOR(S)
Susanne Sterbing-D'Angelo

5d. PROJECT NUMBER

5e. TASK NUMBER

5f. WORK UNIT NUMBER

7. PERFORMING ORGANIZATION NAME(S) AND ADDRESS(ES)
MARYLAND UNIV COLLEGE PARK
3112 LEE BLDG
COLLEGE PARK, MD 20742 - 5100 US

8. PERFORMING ORGANIZATION REPORT NUMBER

9. SPONSORING/MONITORING AGENCY NAME(S) AND ADDRESS(ES)
AF Office of Scientific Research
875 N. Randolph St. Room 3112
Arlington, VA 22203

10. SPONSOR/MONITOR'S ACRONYM(S)
AFRL/AFOSR RTB2

11. SPONSOR/MONITOR'S REPORT NUMBER(S)
AFRL-AFOSR-VA-TR-2018-0362

12. DISTRIBUTION/AVAILABILITY STATEMENT
A DISTRIBUTION UNLIMITED: PB Public Release

13. SUPPLEMENTARY NOTES

14. ABSTRACT
Goal of this project is to deepen our understanding of sensorimotor feedback control in bat flight. This effort led to a description of sensor-guided flight that can be transitioned to autonomous micro-air vehicles and other aircrafts.

15. SUBJECT TERMS
adaptive flight control

16. SECURITY CLASSIFICATION OF:			17. LIMITATION OF ABSTRACT	18. NUMBER OF PAGES	19a. NAME OF RESPONSIBLE PERSON
a. REPORT	b. ABSTRACT	c. THIS PAGE			BRADSHAW, PATRICK
Unclassified	Unclassified	Unclassified	UU		

19b. TELEPHONE NUMBER *(Include area code)*
703-588-8492

Standard Form 298 (Rev. 8/98)
Prescribed by ANSI Std. Z39.18

Multisensory Integration for Adaptive Flight Control in Bats - Final Report

Contents

Multisensory Integration for Adaptive Flight Control in Bats - Final Report

I. Project Report

Goal of this project is to deepen our understanding of sensorimotor feedback control in bat flight. This effort led to a description of sensor-guided flight that can be transitioned to autonomous micro-air vehicles and other aircrafts.

1. Comparative analysis of tactile hairs on the wing membrane of four bat species

Bats are the second-largest group of mammals, with over 1300 species, and they are the only mammals with powered flight. The bat wing is covered with microscopically small, tactile hairs that have been shown to be involved in sensing air flow for improved flight maneuverability in two bat species, the frugi-/nectarivorous *Carollia perspicillata*, and the insectivorous *Eptesicus fuscus* (Sterbing-D'Angelo et al., 2011). The bat's wing membrane is unusually thin, and is lacking glabrous skin, which is typically found on the ventral surface of the hands of other mammals. Hence, wing hairs are found on both the dorsal and ventral sides of the hand.

Bats live in a wide variety of habitats, and their flight requirements are very diverse. With the goal of characterizing wing hairs in bat species with diverse flight behaviors, we studied the hairs on the wing membrane of four very different species: the insectivorous big brown bat, *Eptesicus fuscus* (*E.f.*, Vespertilionidae, Palisot de Beauvois, 1796), the frugi-/nectarivourous short-tailed fruit bat, *Carollia perspicillata* (*C.p.*, Phyllostomidae, Linnaeus, 1758), the sanguivorous vampire bat, *Desmodus rotundus* (*D.r.*, Phyllostomidae, Saint-Hilaire, 1810) and the frugivorous Egyptian fruit bat, *Rousettus aegyptiacus* (*R.a.*, Pteropodidae, Geoffroy, 1810); Sterbing and Moss, *J. Mammology*, in review. These bat species exhibit different flight specializations due to their particular diets and habitats, and cover a wide range of body mass and subsequently wing loading, which is the quotient of body mass and wing area.

The bat wing is a highly adaptive airfoil that enables demanding flight maneuvers, which are performed with an astonishing robustness under turbulent conditions, and stability at slow flight speeds. Particle imaging velocimetry studies revealed that bat flight generates complex aerodynamic tracks with wake vortices, i.e., areas of turbulent, reverse air flow, mainly along the dorsal leading edge and trailing edges of the wing (Muijres et al., 2008). Neurons in somatosensory cortex of *E.f.* mostly show directional responses to airflow, preferring reverse airflow as caused by the dorsal leading edge vortex during slow flight (Sterbing-D'Angelo et al. 2011, Sterbing-D'Angelo et al. 2016, Muijres et al. 2014). Hence, our hypothesis was that the wing hair morphology and distribution of hairs might show species differences, such as body mass, wing span, aspect ratio, wing loading, or flight speed.

Materials and Methods: *Animals-* All tissue used in this study was collected from freshly euthanized bats with intact wings used for other studies in our group. *Eptesicus fuscus* were wild-caught in Maryland under a permit from the Maryland Department of Natural Resources. *Carollia perspicillata,* native to Central America, imported from the Montréal Biodôme, Canada, the *Desmodus rotundus* wings were provided by the Wilkinson lab at the University of Maryland, and the Egyptian fruit bats were imported from the Weizmann Institute of Science, Rehovot, Israel, both under permits from the Center for Disease Control. Bats were housed under reversed 12 hour light/dark conditions. *Carollia perspicillata* and *Rousettus aegyptiacus* were maintained on a diet of various fruits and water. *Eptesicus fuscus* were maintained on a diet of mealworms, *Tenebrio molitor,* and water. Husbandry and procedures were approved by the

2

University of Maryland Institutional Animal Care and Use Committee and overseen by the US Department of Agriculture.
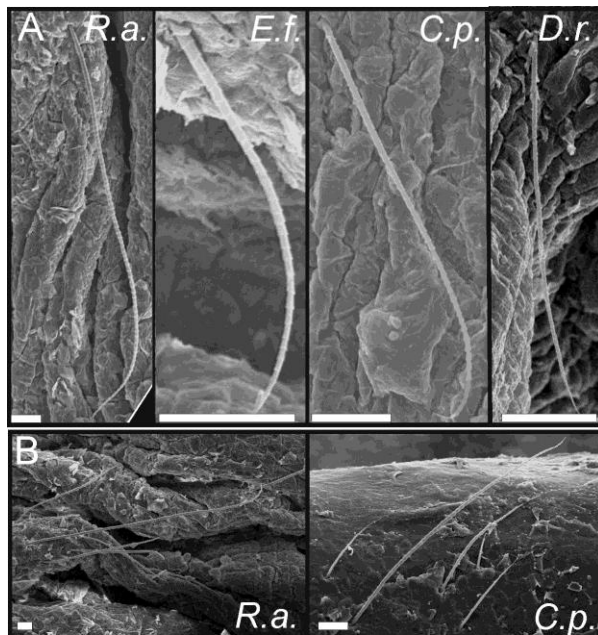
Scanning electron microscopy - Circular samples (13 mm diameter) from 26 different parts of the dorsal and ventral wing of three *Eptesicus fuscus*, 24 samples from the wings of two *Carollia perspicillata*, and 44 of two *Rousettus aegyptiacus* at corresponding locations, were taken and fixated in 2.5% glutaraldehyde solution, washed in phosphate buffer solution (PBS), and then fixated in 1% osmium tetroxide in PBS (60 min). After standard washing procedure with bi-distilled water, and dehydration in 75%, 95%, and 100% ethanol, the samples were dried in a critical point dryer (Denton DCP-1, Moorestown, NJ, USA). The samples were mounted onto metal pedestals with silver paste, placed in a 50°C oven to harden, and then coated with gold palladium alloy (Denton DV-502/502 Vacuum Evaporator, Moorestown, NJ, USA). The samples were viewed in a scanning electron microscope (Amray AMR-1610, Bedford, MA, USA). Only intact, and fully visible hairs were included in the taper measurements, which – given the sparse distribution of these hairs - reduced the sample to 111 hairs from *Eptesicus fuscus*, 132 hairs from *Carollia perspicillata*, and 121 hairs from *Rousettus aegyptiacus*.

Results: Table 1.1. lists morphological parameters that are important for flight, e.g., body mass, wing span, wing aspect ratio, and wing loading for the four species. Although body mass and wingspan of *E.f.* and *C.p.* are very similar, the aspect ratio is higher, and wing loading slightly lower in *E.f.* Low body mass in combination with large wings has been discussed as being correlated with high maneuverability as indicated by minimum turn angles the bat can produce (Norberg and Rayner 1987). The higher the aspect ratio, the longer and narrower is the wing; such a wing shape is typically found in fast-flying bats that hunt for insects in open space. Wing aspect ratio typically ranges from 5 to 14 in echolocating bats, and wing loading ranges from about 4.1 to 28 N/m^2, with large species having the highest loading values (Norberg, 1994; Farney and Fleharty, 1969; Lawlor, 1973). Hence *R.a.* and also *D.r.* are close to the upper end of the wing loading spectrum, and *E.f.* and *C.p.* at the middle range.

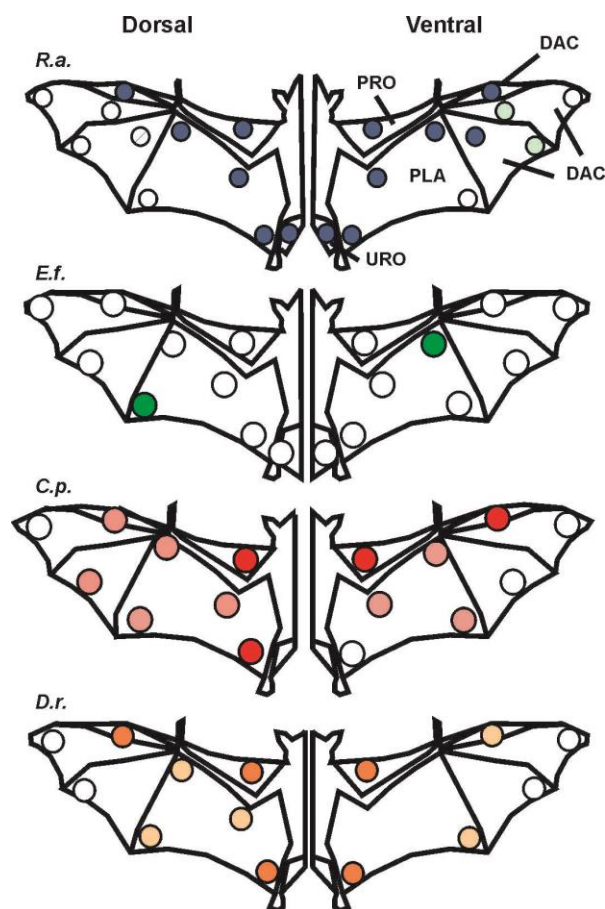| Species	Body Mass (g)	Wing span (cm)	Aspect Ratio	Wing loading (N/m^2)
E.f.	16	32	6.4	9.4
C.p.	19	32	6.1	11.4
D.r.	31	37	6.8	19.6
R.a.	140	57	5.9	24.6

Table 1.1. Species characteristics. Body mass, wingspan, wing aspect ratio (wingspan^2 / wing area), and wing loading (body mass / wing area) of the three bat species. *E.f.: Eptesicus fuscus, C.p.: Carollia perspicillata, D.r.*: *Desmodus rotundus*, *R.a.: Rousettus aegyptiacus.*

Scanning electron microscopy - Wing membrane samples were collected from the dorsal and ventral propatagium (leading edge of the wing in front of the arm), from different locations along the leading and trailing edge of the dactylopatagium, the membranes between the fingers, and the medial portion and trailing edge of the plagiopatagium, the membrane between finger 5 (D 5) and the body/leg in all four species, as well as the uropatagium (tail membrane) in *R.a.* and *E. fuscus*. The phyllostomid species (*D.r.* and *C.p.*) have a very short tail, and subsequently the uropatagium is reduced to a narrow band of

Figure 1.1. Scanning electron microscope photomicrographs of wing hairs. (A) Shown are hairs from the dorsal dactylopatagium of the four species, *Rousettus aegyptiacus (R.a.)* left, *Eptesicus fuscus (E.f.), Carollia perspicillata (C.p.), and Desmodus rotundus (D.r.)*. (B) Group of hairs on the dorsal dactylopatagium of *Rousettus aegyptiacus* and *Carollia perspicillata.* The white bars indicate 50um.

membrane, which could not be sampled with the required surface area. In all four species, the SEM analysis of the wing membranes revealed that there are two populations of hairs on the wing, short, regularly distributed hairs, and longer, up to several mm long, densely, but irregularly distributed hairs found along the limbs, especially on the ventral side of the wing close to the body, and in *R.a.* as well as *E.f.* also on the ventral and dorsal uropatagium. In contrast to the short hair, the long hair type is approximately between 3 and 10 times longer, larger in diameter, and less tapered. The fur hair typically has a spiny coronal or imbricate scale pattern, and is easily distinguishable from the much smaller tactile wing hair. Figure 1.1.A (SEM photographs) shows examples of single, short hairs found on the dorsal dactylopatagium in the four species. Figure 1.1.B shows groups of hairs found on the ventral dactylopatagium of *R.a.* (left), and on the dorsal dactylopatagium *C.p.* (right). In *C.p.*, the different areas of the wing membrane are equipped with either single hairs, or with a mix of single hairs and small groups of 2-5 hairs (tufts), or only with grouped hairs.

Figure 1.2. Locations of wing membrane samples collected from four species of bats. Dorsal locations are shown on the left, ventral locations on the right. Hollow circles mark locations, where only single hairs were found, light colored circles mark locations that had a mix of single hairs and grouped hairs. Dark colored circles indicate locations with mostly tufts. The locations marked green in *E.f.* contained pairs of hairs. DAC - dactylopatagium, PLA - plagiopatagium, PRO -propatagium, URO - uropatagium.
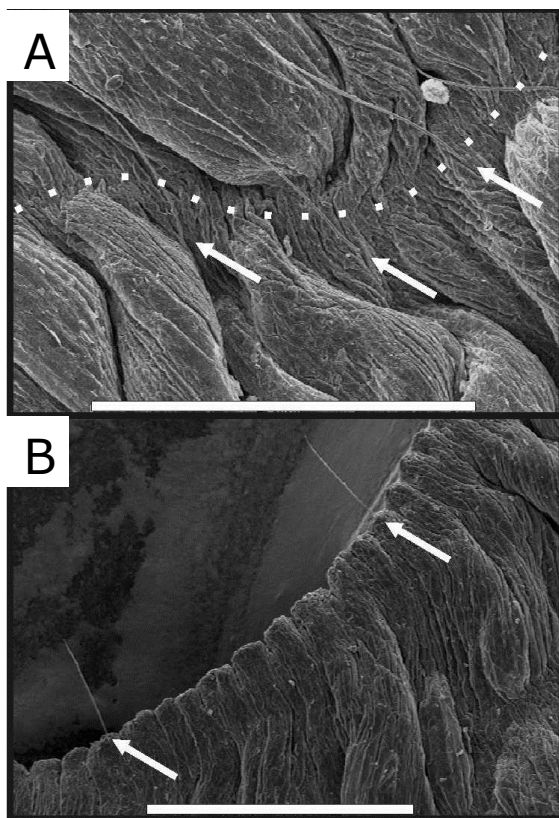
Figure 1.3. (A) Hairs – marked with arrows- next to an elastin band (dotted line) on the dorsal plagiopatagium of *D.r.* (B) Hairs on the very caudal edge of the dactylopatagium of *D.r.* The white bars indicate 1 mm.

Typically, the hairs within groups are of different length. These groups are found on the dorsal and ventral wing surfaces except the dorsal wing tip and along most of the ventral trailing edge.

In *R.a.* and *D.r.,* groups or tufts of 2-7 hairs are found in similar areas as in *C.p.,* but also in additional regions. Tufts of hairs are generally missing in *E.f.,* but 2 hairs protruding from one dome can be found occasionally on the dorsal and ventral plagiopatagium of this species (Figure 1.2.). These findings were consistent between all examined individuals of the same species. The regularly distributed short hairs are strongly tapered, only few um thick at the base (means +/- *SD*: *E.f.*: 4.59 um +/- 0.94 um; *C.p.*: 5.03 um +/- 1.03 um; *R.a.*:11.04 um +/- 3.31 um, *D.r.*: 7.85 um +/- 2.66 um.

The hairs end in a thin wisp that is less than 1 um in diameter in the three laryngeal echolocators (means: *E.f.*: 0.8 um; *C.p.*: 0.63 um; *D.r.*: 0.72 um), but in a more blunt tip of 4.68 um in *R.a*. Overall, 479 hairs were morphologically analyzed, 132 in *C.p.*, 108 in *E.f.*, 121 in *R.a.*, and 118 in *D.r.* Often, but not always those hairs are found along the elastin bands that run through the wing membrane (Figure 1.3.A). The hairs can also be found in membrane regions away from elastin bands, over bone structures, as well as a "fringe" at the very edge of the membrane (Figure 1.3.B) in all species. Each hair scale consists of only one follicle cell resulting in a simple, smooth coronal pattern (Debelica and Thies, 2009). The average density of the wing membrane hairs is low with about 1 to 3 hairs per mm^2 membrane surface on the dactylopatagium and plagiopatagium in all species, but can be considerably higher in some areas close to the arm on the propatagium of the larger species *R.a.* and *D.r.*The hair density is lower along the trailing edge of three bat species, except in *C.p.* It does not significantly vary between the leading and trailing edge samples in *R.a.* and *D.r.* (Figure 1.4.A), Figure 1.4.B illustrates that the mean length of the hairs varies between leading edge (propatagium, and rostral dactylopatagium including wing tip) and trailing edge (caudal plagiopatagium and dactylopatagium) locations (data from both surfaces pooled). All four species show a significant hair length decrease between leading edge and trailing edge. Figure 1.4C shows that the hair length correlates well with the wing loading value of each species for both the leading and trailing edge.
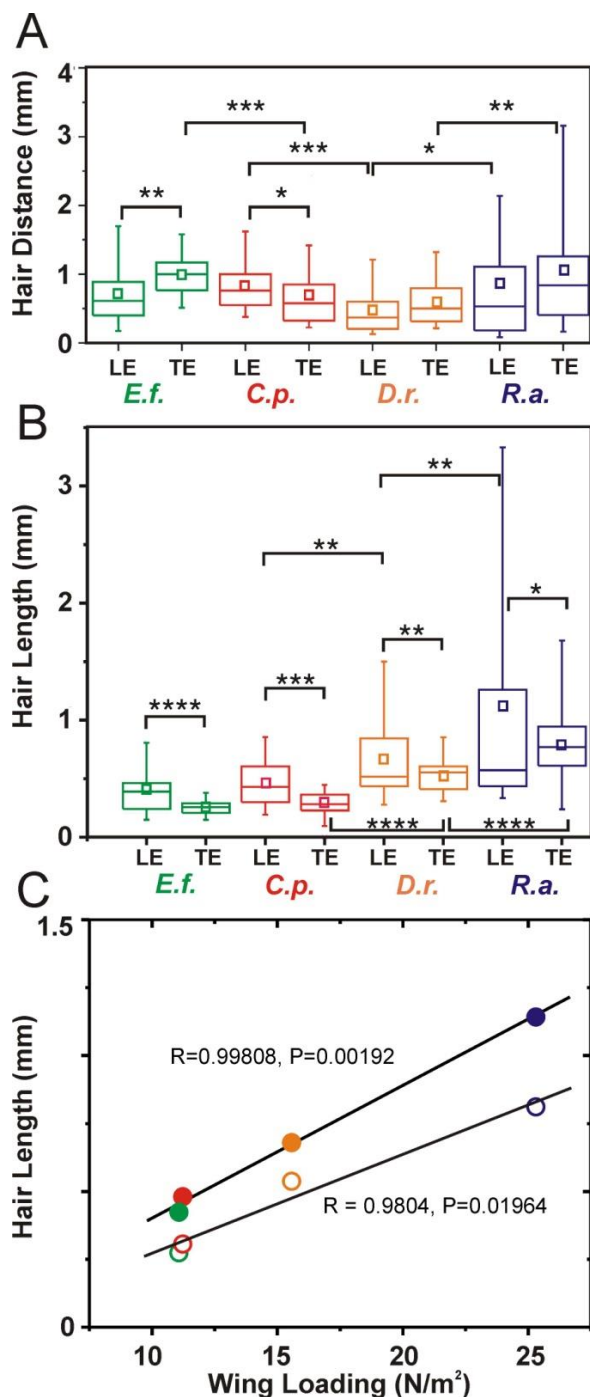
Figure 1.4. A: Mean distance between hairs compared for leading edge (LE) versus trailing edge (TE) of the bat wing of the four species, *Rousettus aegyptiacus (R.a.)* left, *Eptesicus fuscus (E.f.), Carollia perspicillata (C.p.), and Desmodus rotundus (D.r.)*. Mean (small squares), median (horizontal line in box), interquartile range (box), 5th and 95th percentile (whisker). ANOVA Significance levels: *: P <= 0.05, **: P <= 0.01, ***:P <= 0.001, ****: P<= 0.0001 (Bonferroni correction for multiple comparisons, Levene tests for equal variance). B: Mean length of the hairs on LE and TE wing regions. Graph organization same as A. C: Leading edge (solid circles) and trailing edge (hollow circles) hair length plotted versus wing loading of the four bat species, *E.f.* (green), *C.p.* (red), *D.r.* (orange), *R.a.* (blue). For both the LE and TE hair length correlates with wing loading (linear regression, R and P values next to regression lines).

Figure 1.5.A shows the distributions of hair tip and base diameters from all hairs (entire dorsal and ventral surface) sampled from the four species. Base and tip diameter are plotted on a logarithmic scale for clarity. The x marks the median, the ellipse the area of standard deviation. The hair taper analysis, which takes hair length into account, revealed that *R.a.* hairs are the least tapered (Figure 1.5.B). Interestingly, the taper of the closely related phyllostomids *C.p.* and *D.r.* are not statistically different (ANOVA, P = 0.2702), although these species differ substantially particularly in hair base diameter, body size (Table 1.1), and life style. The largest statistical differences are found for all three parameters, base diameter, tip diameter, as well as taper, when *R.a.* (Yangochiroptera, formerly grouped as Megachiroptera) is compared with the three laryngeal echolocators (Yinpterochiroptera, formerly grouped as Microchiroptera). For significance levels see figure caption.
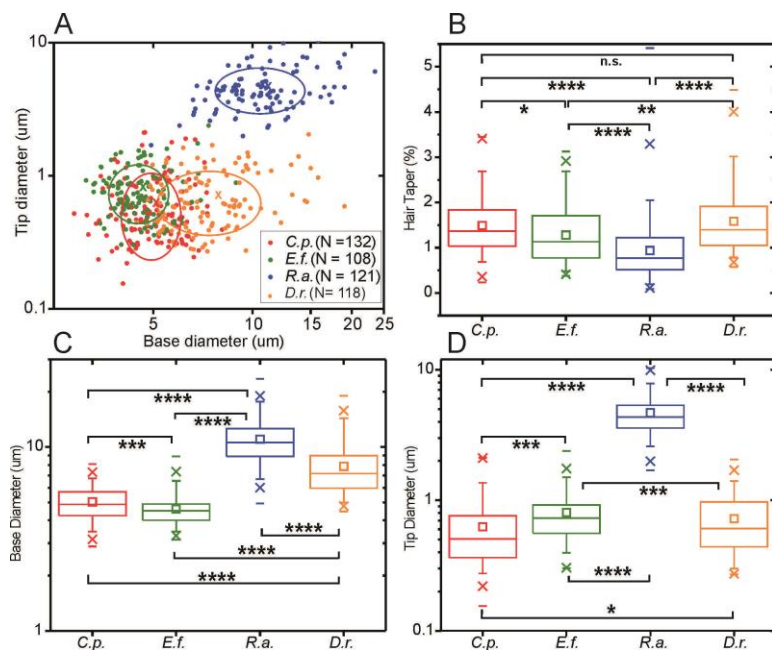
Figure 1.5. Morphological parameters of wing hairs in four bat species. A: Base and tip diameter of the hairs in um, plotted on logarithmic axes for clarity. The x marks the mean for each species. The ellipse indicates the standard deviation. B: Mean (small squares), median (horizontal line in box), interquartile range (box), 5th and 95th percentile (whisker), 1%, 99% percentile (X), min/max values (small horizontal bars) of the hair taper in % across species. C: Same statistical measures for the hair base diameter, and D: for the hair tip diameter. Significance levels: *: P <= 0.05, **: P <= 0.01, ***:P <= 0.001, ****: P<= 0.0001 (Bonferroni correction for multiple comparisons, Levene tests for equal variance). Comparisons not indicated are not significant at 0.05 level.

Discussion - We found two distinct types of hairs on the bat wing, a longer fur-like (pelage) hair that is found close to limbs and body of the animal, and a very short, strongly tapered type of hair, which is found on almost all membranous parts of the wing, also on the ventral wing surface. Finding hairs on the ventral dactylopatagium in all four species is of particular interest, because in other mammals the ventral side of the hand is glabrous, hence free of hair. This finding indicates that the processes during embryological development of the dactylopatagium, which derives from embryonal interdigital webbing that is not subject to apoptosis in bats (Weatherbee et al. 2006), also promotes hair growth. It has been described that inhibiting bone morphogenetic protein signaling, which plays an important role during early skeletal formation, triggers ectopic hair development on glabrous skin in mice. Therefore, the anti-apoptotic mechanisms that govern wing membrane formation in bats might also account for its unusual expansion of hair follicles on the ventral surface as an evolutionary adaptation for airflow sensing (Mayer et al. 2008). Furthermore, the hairs found on the plagiopatagium, which grows out of the flank of the embryo, and finally attaches to digit 5 (Cretekos et al. 2005), do not differ morphologically from the hairs found on the dactylopatagium. The pelage hair type does not protrude from a dome-like structure like the short hairs found on the wing. According to Bullen and McKenzie (2008), these long hairs might smooth the contour of the bat in wing regions that have sharp angles, e.g., close to the trunk, arms and legs, and therefore passively improve aerodynamics of the flying bat by reducing drag. The short hairs are so sparsely distributed that viscous coupling between single hairs can be excluded (Lewin and Hallam 2010), unless the hairs protrude from the same dome, such as the groups/tufts of hairs, which we found frequently in 3 of the four species we studied. In any case, the distance between the groups/tufts is similar to the distance between single hairs, and therefore large enough to avoid viscous coupling between the groups, which might function collectively as sensory units, and preliminary data suggests that hair groups/tufts may share the receptor substrate of the dome. Further investigations are needed to confirm this observation. Interestingly, the only insectivorous vespertilionid species included in this study did not show

significant grouping of hairs, while the phyllostomids and the Egyptian fruit bat had grouped/tufted hairs over a large wing area, indicating that body mass or bat family does not seem to be a factor. It is noteworthy that a larger, insectivorous vespertilionid bat, the pallid bat, *Antrozous pallidus* (20 - 35 g), also shows groups of hairs protruding from single domes (Zook and Fowler 1986).

Functionally, the short length of the bat wing hairs makes them very suitable for responding to boundary layer flow, close to the membrane surface where the air is viscous (Dickinson, 2010). A sharp taper has functional implications: it assures that the breakage point of the hair is very close to the tip. Hence, the mass of the hair does not change significantly when breakage occurs (Williams and Kramer 2010). According to Dickinson's (2010) modeling results, linearly tapered hairs provide greater output sensitivity than hairs of uniform cross-section. Dickinson further concluded that the computed optimal hair lengths are in agreement with the range of hair lengths in different bat species, *Eptesicus fuscus, Glossophaga soricina, and Pteropus poliocephalus.* These modeling results support the hypothesis that bats use tactile hairs to detect changes in boundary layer shape (Dickinson 2010). We further suggest that the hairs within multi-hair tufts, which typically have different lengths, are well suited to monitor shear in different sublayers of the boundary layer flow, i.e., in the viscous and the buffer layer at the same location. Common to all four bat species in the present study is the finding that microscopic tactile hairs are significantly shorter close to the trailing edge of the wing compared to the leading edge. They also are stiffer than the hairs at the leading edge of the wing (Sterbing-D'Angelo et al. 2016). This finding suggests that it might be advantageous to limit the hair length to fall within airflow sublayers along the trailing edge (e.g., viscous layer, buffer layer, turbulent layer). In general, hair length correlated with body mass and wing loading values of the species, i.e. larger species have longer hairs. This is to be expected, because the thickness of the boundary layer depends on the Reynolds number, the product of air flow velocity and chord length divides by the kinetic viscosity of air Hence, at a given flow velocity and viscosity, the Reynolds number increases with the rostro-caudal (chord) length of the wing.

We frequently observed broken tips in bat wing hairs in the SEM analysis, and as predicted by the taper, breaks were always found at one of the most distal segments, thereby only negligibly changing a hair's mass. A hair was classified as intact by the species-specific tip diameter and, most importantly, by the shape of the last segment, which is elongated in intact hair. Only fully intact hairs were included for the taper measurements in this study, and it is unclear whether the observed breaks occurred before or after tissue preparation for the scanning electron microscopy.

In summary, the present study shows that sparse grids of short tactile wing hairs are ubiquitously found in a variety of bat species, and their anatomy and distribution across the wing membrane show little variation, in spite of the very different embryonic origins of wing membrane segments and flight specializations of the four species included in these studies. The dimensions of the hairs correlate best with wing loading and body mass, when compared across species. In all species, hairs located along the trailing edge are significantly shorter than those on the leading edge of the wing on both the dorsal and ventral surfaces. The length of the wing hairs appears to be scaled to the average boundary layer thickness of each bat species.

2. Mechanical properties of tactile wing hairs - Laser scanning vibrometry

The bat wing is sparsely covered with microscopically small, sensory hairs that have been shown to be involved in sensing airflow for improved flight maneuverability in two bat species, including the big brown bat, *Eptesicus fuscus* (Sterbing et al. 2011). The bat's wing membrane is unusually thin, and is lacking glabrous skin that is typically found on the ventral surface of the hands of other mammals. In other words, hairs are found on both the dorsal and ventral sides of the bat's hand-wing (Marshall et al 2015). Chitinous, airflow-sensing sensilla on the wing and other body parts of insects have been shown to play a role in flight control (Pfluger & Tautz 1982, Ai et al. 2010, Dickinson 1990), as have vibrotactile receptors at the feather base of birds (Necker 1985, Horster 1990). Experiments with tethered flies revealed that they use mechanosensors on the antennae to regulate wing motion in response to changes in airspeed (Gewecke & Schlegel 1970, Budick et al. 2007, Mamiya et al. 2011, Fuller et al. 2014). Movement is detected by the Johnston organ and a campaniform sensillum located between the second and third antennal segments (Burkhardt & Gewecke 1965)]. In hawk moths, the antennae are used for additional flight control aspects in reaction to body rotation, which are mediated by halters in flies (Sane et al. 2007, Hinterwirth & Daniel 2010).

In birds it has been well established that mechanoreceptors associated with feathers (Herbst corpuscles, Merkel cell receptors) influence bird flight. Air currents directed to the breast feathers influence flight pattern (Gewecke & Woike 1978). Brown and Fedde (1993) found a strong relationship between the vertical feather angle and the neuronal spike frequency of both slow and fast adapting mechanoreceptors located at the base of 'hair-like', secondary feathers (filoplumes). They suggested that receptors distributed across the wing from shoulder to wing tip could provide information that would allow the bird's central nervous system to detect stall. Since the airspeed over the wings fluctuates during the wing beat cycle, the instantaneous input from the receptors could provide the central nervous system with information about wing velocity, which is the critical factor in lift generation. As a second mechanism, general velocity information could be obtained by averaging the airspeed velocity over the wings during each wing beat cycle, or averaged over several cycles. Theoretically, similar processes could operate in bats. While bird feathers consist of beta-keratin (Haake et al. 1984), the sensory hairs in bat wings consist of alpha-keratin, like all mammalian hairs (Khan et al. 2014).

Mammalian sensory hairs, e.g. whiskers, have tactile receptors located in the skin at their follicle (Johnson 2001). So do the hairs on the bat wing (Marshall et al. 2015). On the mammalian hand, one tactile receptor type, the Merkel cell neurite complex, is typically only found on the glabrous palm in touch domes (Johnson et al. 2000). In the bat, the hand serves also as a wing, but lacks glabrous skin. Nevertheless, this hand-wing is very rich with Merkel cells that are surrounding hairs, and which are involved in airflow sensing. A second type of receptor, the lanceolate ending, was found surrounding the follicles of the bat wing hairs as well. This receptor is also in other mammals associated with hairs and reports hair movement by brushing in mice (Abraira & Ginty 2013).

The transmission of a mechanical stimulus to the follicle determines the input of tactile information to the central nervous system. It also depends on the mechanical bending properties of the hairs that act like cantilever beams. Of particular importance is the bending stiffness, defined as the product of Young's modulus (YM) and area moment of inertia (AMI). The AMI can be calculated from the geometry of the hair, but estimation of YM requires an experimental approach. The underlying hypothesis is that the

9

natural frequency of the hairs is correlated with hair length. Since the mechanical properties of bat wing hairs are to date unknown, we conducted contact-free laser scanning experiments of hairs of the big brown bat across the dorsal and ventral wing membrane surfaces, to determine the elastic modulus (YM) and the hair's natural frequencies with respect to their length. The results presented here represent a first step towards understanding the mechanics of tactile hairs in the control of bat flight, and the results can be applied to biomimetic airflow sensors.

Methods: *Animals* - All tissue used in this study was collected from freshly euthanized bats with intact wings used for other studies by our group. *Eptesicus fuscus* were wild-caught in Maryland under a permit from the Maryland Department of Natural Resources. Bats were housed under reversed 12 h light/dark conditions, and were maintained on a diet of mealworms, *Tenebrio molitor*, and water. Husbandry and procedures were approved by the University of Maryland Institutional Animal Care and Use Committee and overseen by the US Department of Agriculture.

Scanning electron microscopy (SEM) - Twenty-six tissue samples (~13 mm diameter) from different parts of both dorsal and ventral wing membranes of three euthanized *Eptesicus fuscus* were taken and fixated in 2.5% glutaraldehyde solution, washed in phosphate buffer solution (PBS), and then fixated in 1% osmium tetroxide in PBS (60 min). After standard washing procedure with bi-distilled water, and dehydration in 75%, 95%, and 100% ethanol, the samples were dried in a critical point dryer (Denton DCP-1, Moorestown, NJ, USA). The samples were mounted onto metal pedestals with silver paste, placed in a 50 °C oven to harden, and then coated with gold palladium alloy (Denton DV-502/502 Vacuum Evaporator, Moorestown, NJ, USA). The samples were viewed in a SEM (Amray AMR-1610, Bedford, MA, USA).

Laser scanning vibrometry - The natural frequency of the bat hair was obtained by acoustically exciting the hair and measuring its velocity response optically via a laser scanning vibrometer (Polytec, Model MSA-400, Irvine, CA, USA). This method has been proven to be effective for determinaton of natural frequencies and bending modulus for microscale and nanoscale structures (Poncharal et al. 1999). In the experiment, first, tissue samples were taken from various locations on the dorsal and ventral wing membrane of two freshly euthanized *Eptesicus fuscus.* The wing membrane is very compliant and anisotropic, and needs to be mounted to be stretched so that the hairs are fully exposed and accessible for the vibrometer measurement. Hence, each sample was 1–3 cm^2 large and mounted on a separate glass slide with tissue glue (Histoacrylic™, Braun Melsungen AG, Melsungen, Germany). The mounting also minimized elastic deformation. There were usually multiple hairs on each tissue sample, and the total number of tested hairs was 43. The glass slide was clamped on a regular microscope stage under the microscope of the vibrometer. For each hair, the laser spot was focused on the hair and later on the supporting tissue to measure the sound-induced deflection. An ultrasound acoustic emitter (Ultra Sound Advice, Model S56, London, UK, frequency range up to 180 kHz) was used to generate a pure tone acoustic signal, which was driven by using the analog output from a data acquisition card (National Instruments, USB-6361, Austin, TX, USA) via an amplifier. The acoustic stimuli were calibrated using a ¼'' condenser microphone (Brüel & Kjær 7016PM, Nærum, Denmark; sensitivity: 2.95 mV Pa^{-1}).

With the laser spot initially focused on the hair near the tip, a frequency sweep of the acoustic emitter was performed. The real-time velocity response of the hair obtained from the vibrometer controller (Polytec, Irvine, CA, USA) and the acoustic stimulus reference signal from the condenser microphone were recorded via the data acquisition card at a sampling rate of 1 MHz for each channel. Discretized

data points for twenty periods were used to calculate the velocity spectra in response to acoustic stimuli (i.e., the transfer function) as follows. Assume the discrete signals of the acoustic stimuli and velocity response are $x_n = A_p\cos(\omega \cdot n \cdot \Delta t + \phi_p)$ and $y_n = A_v\cos(\omega \cdot n \cdot \Delta t + \phi_v)$, respectively, where A_p and A_v are the amplitudes, ϕ_p and ϕ_v are the initial phase constants, ω is the radial frequency, n is an integer number ($n = 0, 1, 2, ..., N - 1$), N is the total number of data points, and Δt is the sampling interval. Then, for the acoustic stimuli, we can use trigonometric identities to

$$A_p \cos(\phi_p) = \frac{2}{N\Delta t}\sum_{n=0}^{N-1} x_n \cos(\omega \cdot n \cdot \Delta t) \qquad A_p \sin(\phi_p) = -\frac{2}{N\Delta t}\sum_{n=0}^{N-1} x_n \sin(\omega \cdot n \cdot \Delta t),$$

obtain and from which we can solve for A_p and ϕ_p. Similarly, we can solve for A_v and ϕ_v for the velocity response. The magnitude of the transfer function can thus be obtained in logarithmic scale as $TF_{dB} = 20\log_{10}(A_v/A_p)$, which has a unit of dB. (The phase of the transfer function is $\phi_v - \phi_p$). The use of acoustic stimuli to excite the hair has the advantage of being remote and non-contact, which has been recently demonstrated for excitation of microcantilevers (Gao et al. 2014).

This process was then repeated when the laser spot was focused on the supporting tissue to obtain the transfer function of the surrounding tissue. Furthermore, the transfer function of each individual hair was subtracted from that of wing membrane tissue surrounding it to find the peak corresponding to the fundamental mode; i.e., the fundamental natural frequency. To confirm the obtained natural frequency is indeed the fundamental natural frequency, measurements of the hair responses at this frequency were conducted at a number of incremental distances to the hair root (10–15 data points) to obtain the mode shape, using the real part of the transfer function, i.e., $A_v/A_p \cdot \cos(\phi_v - \phi_p)$. If the hair displacement is increased monotonically with the distance from the root, the excitation of fundamental mode is confirmed.

Results: *Hair morphology: SEM* - Wing membrane samples were collected from the dorsal and ventral propatagium (leading edge of the wing in front of the arm), from different locations along the leading and trailing edge of the dactylopatagium, the membranes between the fingers, and the medial portion and trailing edge of the plagiopatagium, the membrane between finger 5 (D 5) and the body/leg, as well as the uropatagium (tail membrane, see schematic in Figure 2.1(d)). The SEM analysis of the wing membranes revealed that there are two populations of hairs on the wing: (a) a short (<800 μm), regularly distributed hair (Figures 2.1(a)–(c)), and (b) a second type, up to several mm long. This second type of hair is found close to the proximal limbs, particularly on the ventral side, but not on the flight membrane distant from the limbs or the dactylopatagium. In contrast to the short hair, the long hair type is approximately 3–10 times longer, larger in diameter, and less tapered. The long hair type resembles pelage (fur) hair, which covers the body of the bat, and typically has a spiny coronal or imbricate scale pattern. This hair type is easily distinguishable from the much smaller sensory wing hair, which has a smooth coronal scale (Debelica & Thies 2009), and protrudes from a dome-like structure, which the long hair does not. All measurements presented here were made from short hairs. The length of the short hairs is not normally distributed (Shapiro–Wilk test, $P < 0.000\,00$). The median length is 288 μm with an interquartile range (IQR) from 216 to 470 μm for the pooled hairs from both the dorsal and ventral wing membrane.
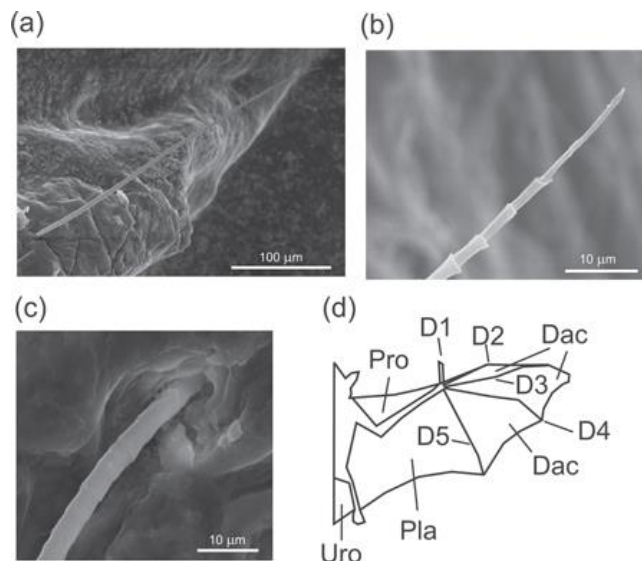
Figure 2.1. (a) SEM photograph of a short (331 μm) wing hair of the big brown bat. Figures 1(b) and (c) show the tip and base of a short hair at higher magnification (see calibration bar). Note the smooth coronal scale pattern clearly visible in (b) and (c). (d) Schematic of a bat wing. D1–5: digits (D1: thumb); Dac: dactylopatagium; Pla: plagiopatagium; Pro: propatagium; Uro: uropatagium.

In the big brown bat, *Eptesicus fuscus*, the short hairs are typically found as rows of single hairs protruding from domes. Tufts of hairs, as described in other species are generally missing in *Eptesicus*, but two hairs protruding from one dome can be found occasionally on the dorsal and ventral plagiopatagium of this species. Neither hair length, nor base and tip diameters are significantly different between the dorsal and ventral wing surfaces (ANOVA, $P > 0.05$, Bonferroni corrected). The hairs are strongly tapered (median 1.25%, IQR: 0.90%–1.76%, $N = 102$). They are only a few μm thick at the base (median: 4.48 μm, IQR: 4.0–4.93 μm, $N = 141$), and end in a thin wisp that is most often less than 1 μm in diameter (median: 0.706 μm, IQR: 0.558–0.911 μm, $N = 108$). For the taper calculations, only hairs with intact tip and unobstructed base were included. We used the following definition to calculate the taper: (base diameter–tip diameter)/(length of hair). This formula assures that taper is normalized for hair length. The taper was the only analyzed parameter found to be different between the dorsal and ventral wing surfaces (ANOVA, $P = 0.015$, Bonferroni corrected), with the dorsal hairs being more sharply tapered (median: 1.54%) than the ventral hairs (median: 1.16%).

The average density of the hairs is low with about 1–3 hairs per mm^2 membrane surface, and also does not differ between the dorsal and ventral membrane. To test whether hairs along the leading edge and trailing edge of the wing show any morphological differences the data set was divided. The leading edge pool included the propatagium and rostral dactylopatagium including wing tip, and the trailing edge included caudal plagiopatagium, uropatagium, and dactylopatagium (data from both the dorsal and ventral surfaces pooled). The distance between a hair and its nearest neighbor differs significantly between the leading (mean: 697 μm) and trailing edge samples (988 μm) with the leading edge being more densely populated (Figure 2(a)). Figure 2(b) illustrates that the median length of the hairs is longer along the leading edge. The hair taper analysis, which takes hair length into account (see definitions above), revealed that the taper is more pronounced in the hairs along the trailing edge.
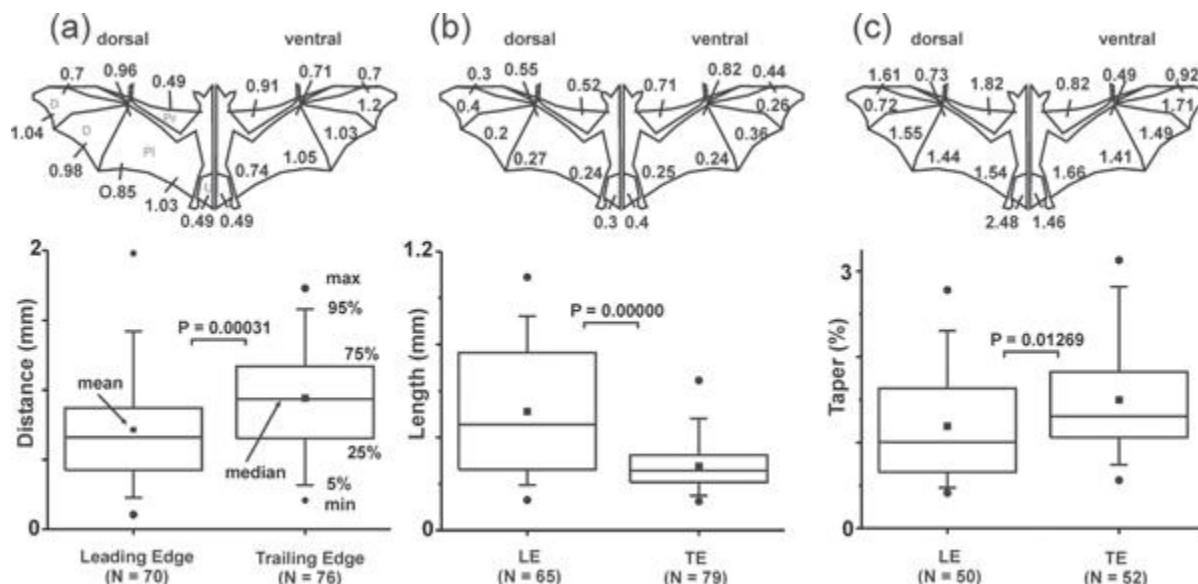
Figure 2.2. Differences between the leading edge (LE) and trailing edge (TE) of the wing. (a) Top panel mean distance between neighboring hairs for various wing locations on the dorsal (left) and ventral (right) surface. D: dactylopatagium, Pl: plagiopatagium, Pr: propatagium, U: uropatagium. Bottom: statistical graph illustrating the difference of the inter-hair distance between LE and TE locations. The inter-hair distance between two neighbored hairs is larger along the trailing edge. (b) Hairs are longer at the LE than at the TE. (c) TE hairs are tapered more than LE hairs. All statistical comparisons were made using one-sided ANOVAS with Bonferroni correction for multiple comparisons, and Levene test for equal variance.

Hair deflection properties: laser scanning vibrometry - Based on past research (e.g., Kan et al. 2013, Hartmann et al. 2003, Quist et al. 2011), we concluded that contact-free deflection measurements of hairs embedded in their supporting tissue can yield the most accurate measurements of their YM, and therefore we chose to use sound stimulation and measure the hairs' deflection and natural frequencies with a laser scanning vibrometer (Figure 2.3(a)). Figure 2.3(b) shows the microscopic image of a representative hair under the acoustic stimulation. The contact-free stimulation avoids changing the mechanical characteristics of the hairs. The natural frequency based method alleviates the needs to accurately measure the input force/pressure and the corresponding deflection. Most important for such a linear system is the relative hair deflection in relation to the excitation frequency. The natural frequencies of the wing hairs were measured this way across samples from both the dorsal and ventral wing surfaces of *Eptesicus fuscus,* selected to match the wing samples that were included in our SEM study. Tissue samples removed from two freshly euthanized *Eptesicus fuscus*. Figure 2.3(c) shows the locations on the wing from which the hairs were sampled (regions 1–6) and the number of hairs for each region, separated for dorsal and ventral surface.
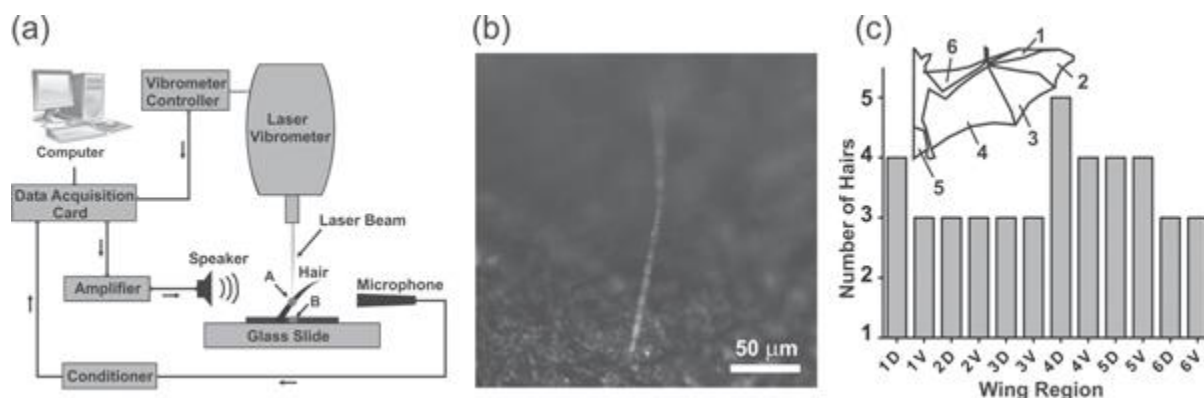
Figure 2.3. (a) Setup for the laser scanning vibrometer measurements. (b) Hair (length about 200 μm), under acoustic stimulation during the measurement. (c) Number of hairs for each location on the wing. D—dorsal wing surface, V—ventral wing surface. The corresponding numbers can be found in the schematic diagram of the bat wing (insert).

The natural frequency of at least 3 hairs on each tissue sample (total of N = 43 hairs) was determined by stimulating each hair acoustically (see methods section). In case that the hair was oriented perpendicularly to the wing membrane, we tilted the entire microscope stage, so that (a) we could see the entire hair, and (b) the vertical component of the velocity could be measured by the vibrometer. Figure 2.3(b) shows a hair under acoustic stimulation. It is clearly visible that the largest deflection occurs close to the hair tip, which appears blurry. The transfer function of each individual hair was subtracted from the transfer function of the surrounding membrane tissue. The transfer function was repeatedly measured at incremental distances to the hair root to confirm that the fundamental mode was excited at the tested frequencies.

Figure 2.4(a) shows the transfer function of an acoustically stimulated hair from the sample. The black line shows the transfer function of the hair, and the gray line the transfer function of the surrounding membrane tissue. Hence the transfer function of the hair is not confounded by the surrounding tissue, and the peak of the transfer function reflects the natural frequency of the fundamental mode. The natural frequencies of hairs from the dorsal surface ranged from 5.18 to 84.5 kHz, and from the ventral surface from 3.7 to 65.8 kHz, and values were normally distributed (Shapiro – Wilk test: P_{dorsal} = 0.159, N = 23; $P_{ventral}$ = 0.784, N = 20). The hair length values were not normally distributed (Shapiro–Wilk test: P_{dorsal} = 0.0014, $P_{ventral}$ = 0.0000). Pooled over the entire wing surface, the mean hair length was not different (P = 0.084 56, α = 0.05, ANOVA) between the dorsal (mean: 281.86 μm, SD: 104.23 μm) and ventral regions (mean: 357.27 μm, SD: 265.69 μm), and neither was the mean natural frequency (P = 0.746, α = 0.05, ANOVA) with a mean of 32.42 kHz (dorsal, SD: 17.77 kHz) and 34.59 kHz (ventral, SD: 16.4 kHz) respectively. Figure 2.4(b) illustrates that the natural frequency decreases with increasing hair length.
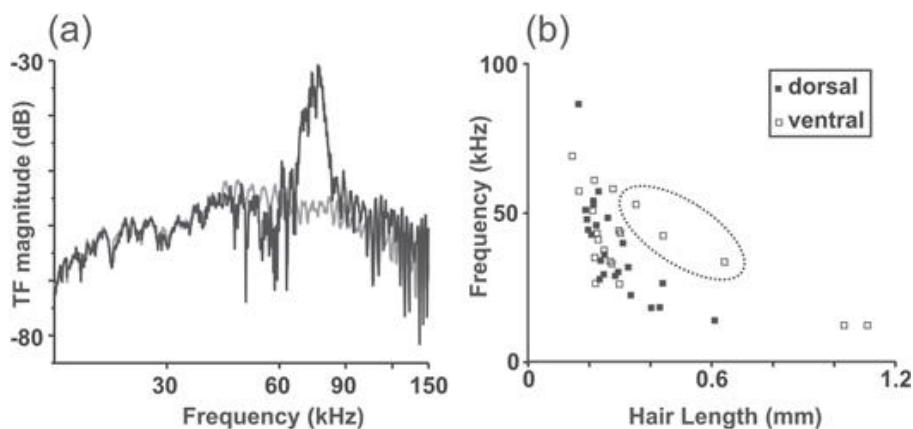
Figure 2.4. (a) Transfer functions of a hair from the wing membrane of *Eptesicus fuscus* in response to a frequency sweep. Black line: transfer function of the hair. Gray line: transfer function of the wing membrane surrounding the hairs. (b) Natural frequency plotted versus hair length for dorsal (filled symbol) and ventral hairs (open symbols). The shorter hairs have a higher natural frequency than longer hairs. Three outliers, all from the ventral wing are circled (standard deviation of the linear fit in (b) >13.8%).

As the gradient of hair length between the leading and trailing edge of the wing suggests, the natural frequencies vary systematically with location on the wing. The natural frequencies are lowest along the leading edge and highest along the trailing edge (Figure 2.5). This difference is significant for both the dorsal ($P = 0.000\ 11$, ANOVA) and the ventral surfaces ($P = 0.008\ 30$, ANOVA). The lowest natural frequencies were found on the dorsal and ventral propatagium, and the highest along the trailing edge of the dactylopatagium between digits 4 and 5.
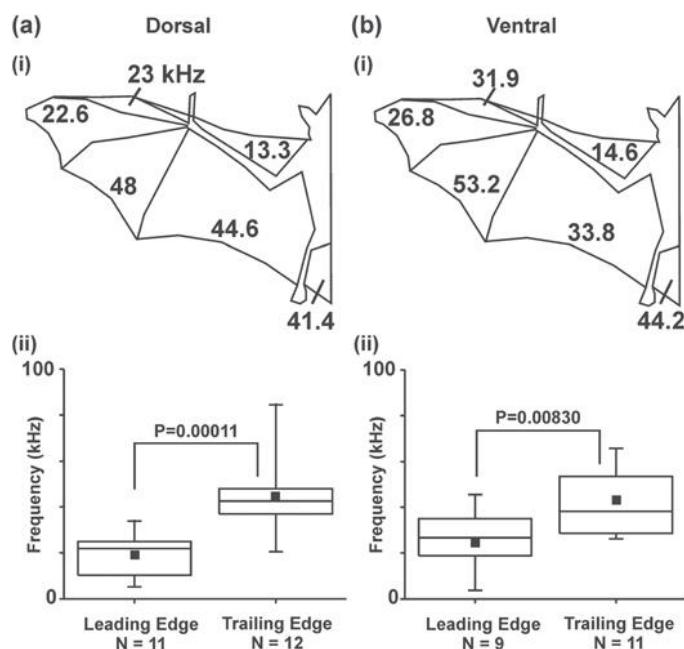

Figure 2.5. (a) Median natural frequencies across the dorsal wing of *Eptesicus fuscus* (i). The natural frequencies along the trailing edge of the wing are higher than those along the leading edge. (b) Same analysis as in (a) for the ventral surface of the wing.

Hair stiffness: calculation of YM - Assuming that the hair behaves like a cantilever beam with a uniform circular cross section, the relationship between the natural frequency f and the length L is as follows [27]:

$$f = \frac{1.8751^2}{2\pi} \frac{d}{L^2} \sqrt{\frac{E}{\rho}}, \qquad (1)$$

where d, E, and ρ are the hair diameter, YM, and density, respectively. To estimate the YM, we plotted the measured natural frequency as a function of L^{-2} (Figure 2.6(a)) for 43 hairs and then used a linear fit between f and L^{-2} ($f = \beta L^{-2}$) to get its slope as $\beta = 1.27 \times 10^6$ (kHz μm^2) with an uncertainty of 13.8% (standard deviation). Furthermore, the hair's YM E could be calculated as:

$$E = 5.177\pi^2 \rho d^{-2}\beta^2. \qquad (2)$$

For an average hair diameter $d = 5$ μm, and fiber density $\rho = 1320$ kgm^{-3} (α-keratin), the YM of the hairs was obtained to be 4.4 GPa with an uncertainty of 29.5% (standard deviation).
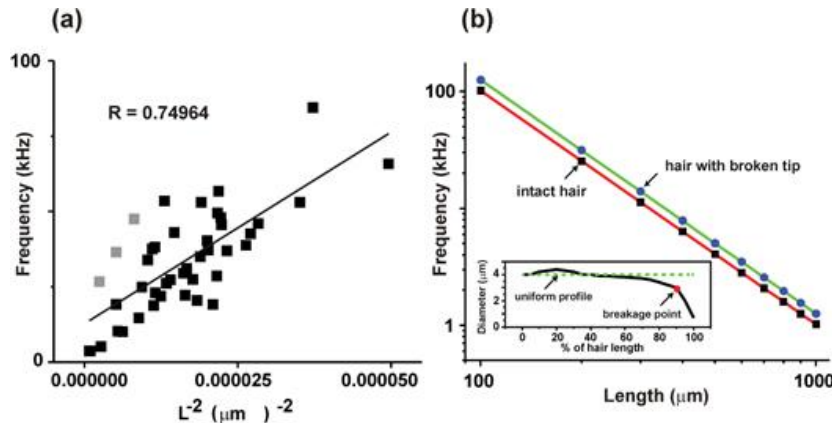

Figure 2.6. (a) Natural frequency is plotted versus L^{-2} for 43 hairs (linear regression, $R = 0.749\,64$, $P < 0.0001$), the 3 outliers marked in Figure 2.2(b) are included (gray squares). (b) Natural frequency of the bat hair calculated by a finite element model as a function of hair length. The inset shows the measured profile of a typical bat hair and where the breakage occurs. The diameter for the uniform profile was taken at the root of the hair. The black squares and blue dots represent the intact hair and the hair with a broken tip, respectively, using the non-uniform profile in the inset; the red and green solid lines are calculated assuming a uniform profile.

Note that bat hair usually has non-uniform profile and is mostly tapered at the tip (see a representative profile shown in the inset of Figure 2.6(b)). To validate the use of uniform cross section for the tapered hair in the above calculation, a finite element model was developed in ANSYS, where the non-uniform cross section of the cantilever beam was specified according to the stepwise measurement of the hair profile. Two scenarios were considered: (i) the hair is intact with a tapered tip (taper starting from 90% of hair length) and (ii) the hair is severed at the breakage point (90% of hair length), and both were compared to the uniform cross section model. Figure 2.6(b) shows the natural frequency obtained as a function of the hair length for these two scenarios based on both uniform and non-uniform profiles. As can be seen from Figure 2.6(b), in both scenarios, the natural frequency obtained by assuming a uniform profile (solid lines) agreed well with that of a non-uniform profile. It should be noted that the hair's natural frequency increases by 23.5% after the breakage occurs, due to the reduced length.

Discussion - Microscopic hairs, sparsely distributed across the bat wing, contribute to airflow sensing for flight control (Sterbing-D'Angelo et al. 2011). Here we provide the first report on the morphology and deflection properties of hairs along the surface of the wing membrane, from the leading to trailing edges. These findings hold relevance to the design and placement of biomimetic airflow sensors.

Short bat wing hairs (<800 μm) are embedded in both the dorsal and ventral wing surfaces. It is noteworthy that the presence of hairs on the ventral dactylopatagium, the membrane spanned between the fingers is unusual, because in other mammals the ventral side of the hand is glabrous, hence devoid of hair. The processes during embryological development of the dactylopatagium, which derives from embryonal interdigital webbing that is not subject to apoptosis in bats (Weatherbee et al. 2006), also promote hair growth. Measurements of length, and tip/base diameters reveal no differences between hairs on the dorsal and ventral surfaces.

Measurements show, however, differences between the short hairs found on the leading and trailing edges of the bat wing. Namely, these wing hairs are longer on the leading edge than on the trailing edge, and show sharper taper on the trailing edge than on the leading edge. A sharp taper has functional implications: it assures that the breakage point of the hair is very close to the tip. Hence, the mass of the hair does not change significantly when breakage occurs (Williams & Kramer 2010). We frequently observed broken tips in bat wing hairs in the SEM analysis, and as predicted by the taper, those breaks were always found at one of the most distal hair segments, thereby only negligibly changing a hair's mass. This was also confirmed by our model that compared several taper models. It should be noted that taper is not calculated consistently in the literature. Some authors refer to the diameter or radius ratio between base and tip of the hair as 'taper'. We used the definition (base diameter–tip diameter)/(length of hair), which normalizes taper with respect to hair length. Only fully intact hairs were included in the taper measurements of this study, and it is unclear whether the breaks occurred before or after tissue preparation for the SEM.The short wing hairs are so sparsely distributed (1–3 hairs per mm^2) that viscous coupling between single hairs can be excluded, unless the hairs protrude from the same dome in the case of groups/tufts of two hairs, which we found only on few locations on the plagiopatagium of the big brown bat, close to digit 5. The hairs within the tufts are separated by about 100 μm or less, which according to models should cause viscous coupling (Bathellier et al. 2005, Lewin & Hallam 2010)). Since they are located within the same sensory dome however, they most likely share the tactile receptor substrate located in the dome, and therefore act as tactile unit. Another, larger, insectivorous vespertilionid bat, the pallid bat, *Antrozous pallidus* (20–35 g body mass) has larger groups of hairs protruding from single domes (Zook & Fowler 1986). Interestingly, the diameter, length and average inter-hair distance along the wing of the bats in our study are quite similar to those found in filiform 'hairs' on the cerci of crickets (diameter: 1– 9 μm, length: 30–1500 μm (Shimozawa & Kanou 1984). Cricket cercal filiform hairs sense velocity, acceleration, and direction of airflow. Measurement of viscous coupling between these filiform hairs revealed that hairs might influence each other up to an inter-hair distance of about 400 μm. Our measurements revealed a mean inter-hair distance of 697 μm (leading edge) and 988 μm (trailing edge). At a given separation, viscous coupling is stronger for hairs of similar length than for those of different length. We found that the average length of the tactile hairs differed significantly between the leading and trailing edge of the wing. Possibly, this length gradient further reduces viscous coupling.

17

Our laser scanning vibrometry measurements revealed that the bat's short wing hairs are very stiff. Their estimated YM is 4.4 GPa, which implies that they would rotate maximally a few micrometers at biologically relevant air speeds, based on the flight speed of *Eptesicus fuscus* (3–10 m s^{-1}). This value is comparable to the YM of rat whiskers, which was found to vary from 1.4 to 7.8 GPa, depending on the measurement method, with resonance methods yielding the highest YM values (Kan et al. 2013, Hartmann et al. 2003, Quist et al. 2011, Adineh et al. 2015). Besides being involved in active whisking for proximal sensing, rat whiskers also respond to passive airflow with directional selectivity (Yu et al. 2016). As predicted by their small dimensions, the wing hairs' natural frequencies are in the ultrasonic range. Depending on the measurement technique (base/tip fixed/fixed versus fixed/free), rat vibrissae show resonance frequencies from 25 to about 750 Hz (Hartmann et al. 2003, Andermann et al. 2004), while the much smaller bat wing hairs showed natural frequencies between 3.7 and 84.5 kHz.

Airflow-sensing 'hairs' of arthropods have similar properties to the short bat wing hairs. For example, the tarsal tactile hairs (trichobothria) of the wandering spider, *Cupiennius salei*, which are used by this animal as tactile sensors in total darkness (Albert et al. 2001), have a YM of 4 GPa, as determined by finite element modeling (Dechant et al. 2001). Their length is about 2600 μm, and their diameter approximately 24 μm. These trichobothria serve to intercept incoming flying prey by detecting the airflow signal generated by small flying insects, e.g. blowflies. These sensors have exquisite sensitivity, and detect airflow velocities from 13 to 81 cm s^{-1} (Klopsch et al 2013). The sensitivity of the primary afferents originating from the bat's wing hairs is unknown to date. However, the response thresholds of cortical (primary somatosensory cortex, SI) multi-neuron clusters to air puff stimuli in the bat (*Eptesicus fuscus)* are comparably sensitive, with thresholds around 20–30 cm s^{-1} (Sterbing-D'Angelo et al. 2011). One has to question, though, whether such a high sensitivity is needed during flapping flight, when airflow velocities are much higher, and well above the average threshold of cortical neurons. The bat's flight velocity under experimental conditions in our flight room ranges between 2 and 4 m s^{-1}, the wing beat velocity ranges around 3 m s^{-1}, and the wing beat rate is 11 Hz on average (Falk et al. 2015). The neurons in SI do not increase firing rate with increasing airflow velocity when stimulated well above threshold (Marshall et al. 2015). They generally exhibit phasic responses, independent of stimulus magnitude or duration, but show high selectivity for the direction of airflow (Sterbing-D'Angelo et al. 2011). These previous findings suggest that the hairs monitor changes in airflow direction rather than wind speed or flight speed.

In addition to the airflow associated with the bat's ground speed, the flapping motion of the wing introduces vorticity (Muijres et al. 2008), which influences the hairs at wing beat frequencies starting around 8–12 Hz. The highest wing beat frequencies occur during slow and hovering flight (~16 Hz), during which the bat uses a greater angle of attack. A recent particle image velocimetry study revealed that bat wing beats generate complex aerodynamic tracts. At the low-end range of the bat's flight speed, particularly during hovering, a prominent leading edge vortex causes reverse airflow close to the dorsal wing surface (Muijres et al. 2008). This vortex also creates additional lift, but it also increases the probability of stall (Muijres et al. 2008). Consequently, neurons in the primary somatosensory cortex of the bat respond more vigorously, when the wing hairs are stimulated with air puffs from the rear, and might therefore be regarded as stall sensors rather than air velocity of flight velocity sensors (Sterbing-D'Angelo et al. 2011).

Two functional regions on the bat wing emerged from the hair analysis: the leading and trailing edges. Hairs along the trailing edge are shorter, are more tapered, and have higher natural frequencies than hairs along the leading edge. They also are more sparsely distributed. Since data about boundary layer airflow

close to the bat wing membrane surface are not yet available, the functional role of these different hair populations remains rather speculative. The different hair properties could be regarded as adaptations to different regional airflow patterns along the chord. The laser scanning vibrometry and mechanics model revealed that the bat wing hairs are very stiff and have an YM comparable to airflow sensing structures of arthropods or rat vibrissae. Further investigations will be conducted to characterize the transduction mechanism of these hairs.

Published: Sterbing-D'Angelo, S.J., Liu, H., Yu, M. and Moss, C.F., 2016. Morphology and deflection properties of bat wing sensory hairs: scanning electron microscopy, laser scanning vibrometry, and mechanics model. Bioinspiration & Biomimetics, 11(5), p.056008.

3. Tactile sensors on the wing

Flight maneuvers require rapid sensory integration to generate adaptive motor output. Bats achieve remarkable agility with modified forelimbs that serve as airfoils while retaining capacity for object manipulation. Wing sensory inputs provide behaviorally relevant information to guide flight; however, components of wing sensory-motor circuits have not been analyzed. Here, we elucidate the organization of wing innervation in an insectivore, the big brown bat, *Eptesicus fuscus*. We demonstrate that wing sensory innervation differs from other vertebrate forelimbs, revealing a peripheral basis for the atypical topographic organization reported for bat somatosensory nuclei. Furthermore, the wing is innervated by an unusual complement of sensory neurons poised to report airflow and touch. Finally, we report that cortical neurons encode tactile and airflow inputs with sparse activity patterns. Together, our findings identify neural substrates of somatosensation in the bat wing and imply that evolutionary pressures giving rise to mammalian flight led to unusual sensorimotor projections (Figure 3.1).
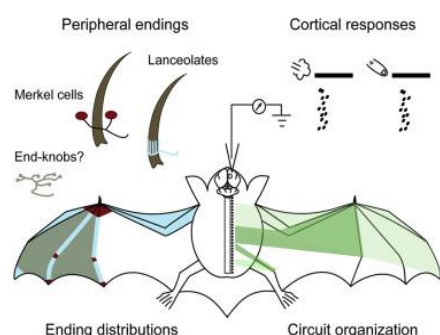

Figure 3.1. Overview schematic. Neural tracers were injected in the wing membrane of E. fuscus. Receptors at the hair base were identified, and the innervation of tactile wing hairs was traced to the spinal dorsal root ganglia.

In Chiroptera, somatotopic maps are atypical, displaying discontinuous representations of body areas and large forelimbs (Calford et al., 1985, Chadha et al., 2011 and Martin, 1993). This suggests that peripheral innervation patterns of the forelimb might differ between bats and other vertebrate species. Shoulder musculature that generates the bat's wing beat has been shown to arise from C5–T1 (Ryan et al., 1997 and Tokita et al., 2012), but sensory innervation of the wing has not been analyzed. To investigate the organization of sensorimotor elements in bat wings, we performed anatomical and functional studies in *E. fuscus*, an echolocating insectivore that displays agile flight.

We hypothesized that bats have unique sensorimotor circuitry that reflects the wing membrane's unusual ontogeny, deriving from the forelimb bud, trunk, and hindlimb. Atypical organization of peripheral innervation should be most evident in the plagiopatagium because it develops through fusion
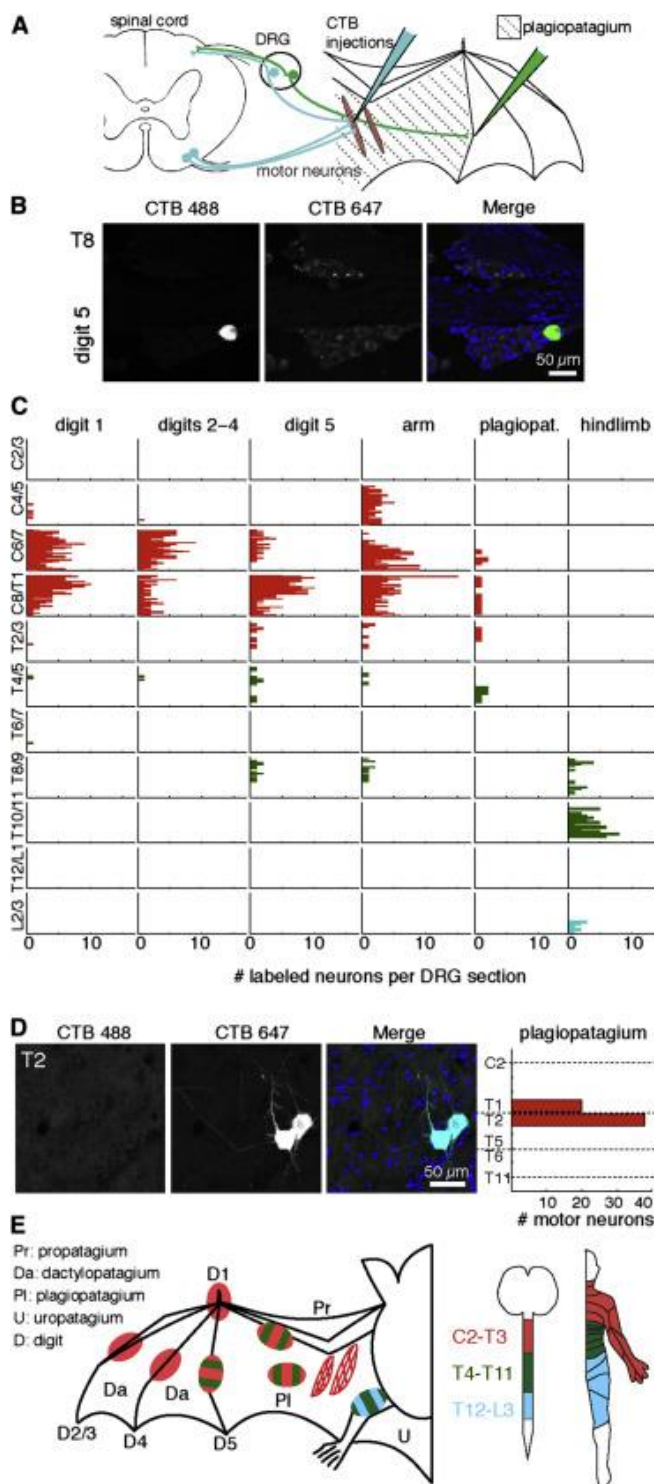
of the forelimb bud and a flank-derived primordium (Weatherbee et al., 2006). The plagiopatagium is the largest part of the wing skin membrane, spanning the area between the fifth digit and body (Figure 3.2A). We performed anterograde neuronal tracing using subcutaneous injections of fluorescent Cholera toxin B (CTB). Focal injections in different wing sites labeled tens to hundreds of DRG neurons. Notably, labeling from individual injections was found in cervical, mid-thoracic, and lower-thoracic DRGs (Figures 3.2B,C). Labeling from digits 1–4 appeared at cervical and upper thoracic levels as observed in other mammalian species; however, for areas surrounding the plagiopatagium, some labeled neurons localized to mid-thoracic DRGs. Labeling from T3–T8 accounted for 4% of DRG neurons innervating the arm, 6% of DRG neurons in digit 5, and 18% of DRG neurons at plagiopatagial sites. Injections in plagiopatagial areas near the hindlimb also revealed atypical innervation, from T8 to T11.

Figure 3.2. Bat Wing Neuronal Tracing Reveals Atypical Somatosensory-Motor Innervation

(A) Schematic of neuronal tracing approach.
(B) T8 DRG section from bat wing injected at digit 5 with CTB Alexa 488 (green). Merged image shows DAPI-stained nuclei (blue).
(C) Histograms show the number of neurons labeled at each spinal level from all injections (≤1.5 µl per injection). Each column shows labeling from a separate wing site (n = 2–3 injections per site from two to three bats). See also Figure S1. Color key in (E).
(D) Motor neurons in upper thoracic spinal cord were labeled by injection of CTB Alexa 647 into plagiopatagial muscles. Merged image shows DAPI-stained nuclei (blue). Right, motor neuron quantification (n = 6 injections in two bats). Dashed lines indicate transection levels of dissected spinal cords. (E) Dermatome and myotome maps. Left, injection sites colored according to spinal level of innervation. Motor pools are represented by hatched areas. Middle, spinal level color key. Right, map of corresponding human dermatomes.

Plagiopatagial muscles tune stiffness of the wing membrane during flight (Cheney et al., 2014). These muscles, which are unusual because they lack bone insertions, derive from forelimb levels (Tokita et al., 2012). To identify spinal motor neurons that innervate the plagiopatagium, we targeted CTB injections to intramembranous muscles. Focal CTB injections showed that >98% of labeled motor neurons extended from levels T1–T3 to innervate plagiopatagial muscles (Figure 3.2D). By contrast, sensory neurons labeled by the same plagiopatagial injections extended from C6 through T5 (Figure 3.2C). Thus, the sensory innervation of the wing extends from a broader segmental range than the motor innervation and arises from lower levels than other mammalian forelimbs (Figure 3.2E). Together, these findings support the hypothesis that the ontogeny of the bat wing, arising from the fusion of the forelimb and plagiopatagial buds, gives rise to atypical innervation patterns in the wing.

We next asked whether the repertoire of somatosensory receptors in wing skin differs from other mammalian limbs. Mammalian forelimbs are replete with morphologically diverse tactile receptors in hairy and glabrous (thick, hairless) skin, some of which have also been reported in bat wings (Ackert, 1914, Yin et al., 2009 and Zook, 2006). Bat wing skin is thin, with two epidermal layers sandwiching the dermis (Swartz et al., 1996). The wing membrane has been proposed to be glabrous skin due to its lack of coat hair (Makanya and Mortola, 2007 and Quay, 1970). Histological analysis revealed that the wing membrane in *E. fuscus* bears two defining features of hairy skin: hair follicles and thin epidermis. These two features are similar in bat wing membrane and mouse hairy skin, although follicle density differs (Figure 3.3A). Thus, we conclude that the wing membrane comprises hairy skin.

We compared sensory endings in bat wing and mouse hairy skin by staining for Neurofilament H (NFH; a conserved marker of myelinated afferents) and peripherin, which is preferentially expressed in small diameter DRG neurons in rodents but appeared to be uniformly expressed in bat DRG neurons (Figure 3.3B). We first examined Merkel cell-neurite complexes, which are innervated by myelinated afferents that report sustained pressure and contribute to shape discrimination (Johnson et al., 2000). In other mammals, Merkel cell-neurite complexes localize to areas of high tactile acuity, including fingerpads, whisker follicles, and touch domes surrounding guard (or tylotrich) hair follicles (Figure 3.3C). In bat wings, Merkel cells were likewise associated with hair follicles and innervated by NFH-positive neurons (Figure 3.3D). The bat epidermis was also innervated by NFH-negative free nerve endings (Figure 3.3E), which mediate nociception and thermoreception in rodent and human skin (Basbaum et al., 2009). Along with these conserved sensory endings, we observed NFH-positive neurons with unusual knob-like endings (Figure 3.3F). These structures resembled end-knobs described in 1914 in bat wing (Ackert, 1914) and Krause end-bulbs, which are proposed to respond to high force levels in glabrous skin of other mammals (Munger and Ide, 1988). These end organs have not been reported in the hairy skin; therefore, these data reveal that a usual combination of sensory receptors innervates bat wings.

We next analyzed how touch receptors are distributed across the wing to provide sensory feedback for behaviors such as food handling, pup cradling, or flight (Figure 3.3G). In vivo injections of fluorescent FM1-43 were used to visualize sensory neurons (Figures 3.3H–J) and Keratin 20 (Krt20) antibodies to stain Merkel cells in whole mount (Figures 3.3K,L; Lesniak et al., 2014 and Meyers et al., 2003). Three sensory receptor types were distinguished by FM1-43 labeling. We observed bright patches, ~50 μm in diameter, termed diffuse endings (Figure 3.3H). These endings were sparse but enriched in inter-digit membranes (Figure 3.3M). Hair follicles, which were innervated by lanceolate endings visible at high magnification (Figure 3.3I), were marked by intense staining, termed punctate endings.
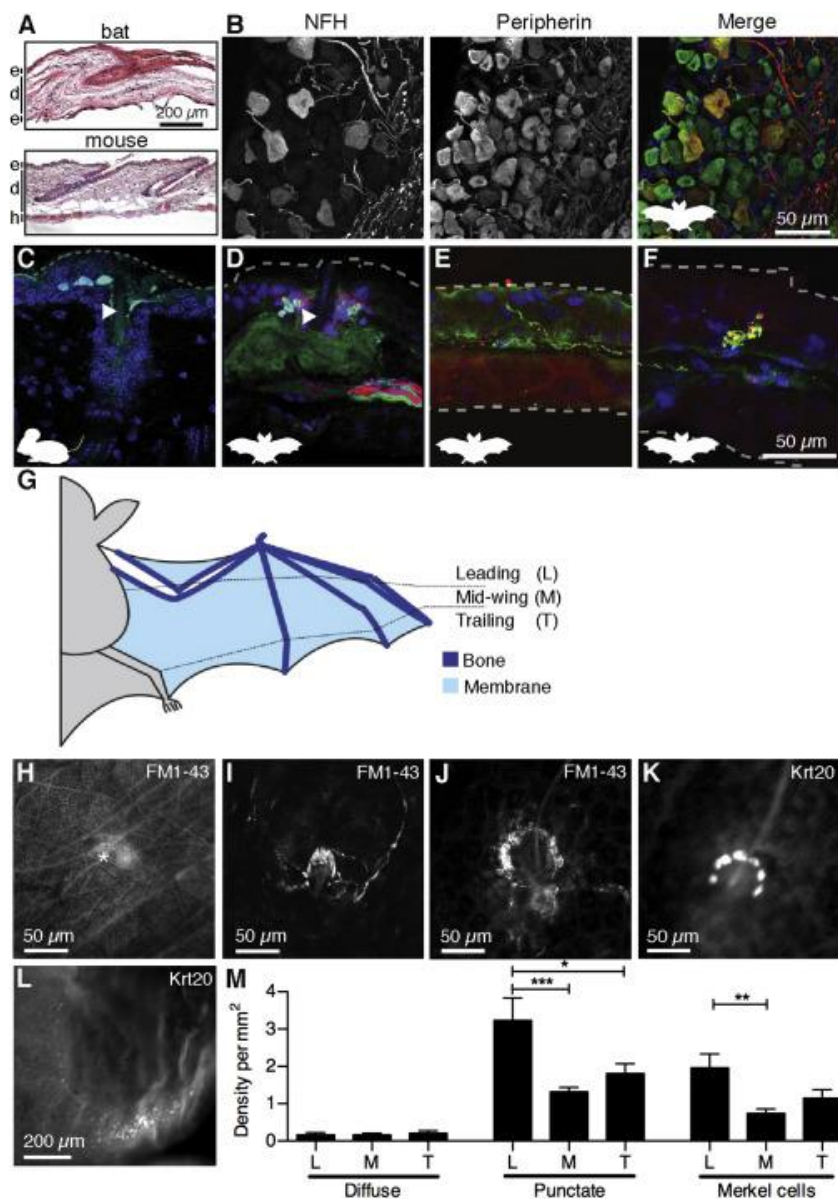
Figure 3.3. An Unusual Repertoire of Touch Receptors Innervates Bat Wings

(A) Skin histology of bat wing and mouse limb (epidermis [e], dermis [d], hypodermis [h]).

(B) Bat DRG labeled with antibodies against neurofilament H (NFH; red) and peripherin (green). DAPI (blue) labeled nuclei. Labeling and colors apply to (B)–(F). (C–F) Immunohistochemistry of mouse limb (C) and bat wing skin (D–F). Dashed lines denote skin surfaces. (C) Keratin 8 (Krt8) antibodies (cyan) labeled mouse Merkel cells adjacent to a guard hair (arrowhead). (D) Krt20 antibodies (cyan) labeled bat Merkel cells around a wing hair (arrowhead). (E) Free nerve ending. (F) Knob-like ending. Scale applies to (C)–(F).

(G) Schematic of wing areas.

(H–J) In vivo FM1-43 injections labeled (H) diffuse endings (asterisk), (I) lanceolate endings, and (J) sensory neurons similar to mouse Merkel-cell afferents.

(K and L) Merkel cells were surveyed using whole-mount Krt20 immuno-staining of 12 wing areas. Merkel cells were found near hairs (K) and along fingertips (L).

(M) Sensory ending density at wing areas defined in (G). (n = 4 wings from four bats [diffuse and punctate], n = 4 wings from three bats [Merkel cells]). Punctate endings and Merkel cells were unevenly distributed across wing areas (one-way ANOVA; p = 0.0004 and p = 0.002, respectively). Asterisks denote significance between groups by Bonferroni's multiple comparison test. ***p ≤ 0.001, **p ≤ 0.01, *p ≤ 0.05. Bars: mean ± SEM.

Bat lanceolate endings appear similar to rapidly adapting low threshold mechanoreceptors that report hair movement in mice (Abraira and Ginty, 2013). Punctate hair receptors were enriched along leading wing edges and were more dense over bones than between digits (Figure 3.3M). Finally, superficial sensory arbors formed crescents around some hair follicles (Figure 3.3J). These afferents were comparable to those that innervate Merkel cells in other species. Consistent with this observation, Merkel-cell clusters were usually situated near hair follicles and were distributed across the wing in a pattern similar to that of punctate hair receptors (Figures 3.3K,M). Although Merkel cells associate with only ~2% of rodent hair follicles (Li et al., 2011), almost half (47%) of all wing hairs were juxtaposed to Merkel cells. Thus, many

wing hairs are dually innervated by lanceolate endings and Merkel-cell afferents, which serve as parallel sensory inputs to report hair movement. High Merkel-cell densities were sometimes also observed along digit tips and at knuckles, indicating these receptors are clustered at phalanges (Figure 3.3L). Thus, this systematic survey reveals a differential distribution of sensory endings across the wing.

The anatomical analysis presented here sets up a system that can be used to discover paradigms for how coherent neural circuits form in appendages that derive from multiple embryonic regions. Our observations demonstrate that the evolutionary progression that gave rise to the bat wing membrane has resulted in atypical somatosensory inputs, which have been co-opted to enhance flight control (Sterbing-D'Angelo et al., 2011). Consistent with this notion, mixed cranial and cervical motor projections innervate the propatagium, which evolved independently in birds, bats, and gliding mammals (Chickering and Sokoloff, 1996 and Thewissen and Babcock, 1991). Thus, vertebrate nervous systems have flexibly adapted to accommodate anatomical specializations for flight.

Our findings suggest that the ontogeny of the wing gives rise to the development of unusual tactile circuitry. Whereas the segmental organization of motor neurons is similar to other mammalian forelimbs, sensory innervation by mid- to lower-thoracic DRGs has not been reported in dermatome maps. This expanded innervation is not simply due to the enlarged size of the wing. Instead, mammals with larger forearms typically have larger sensory ganglia at brachial levels, rather than an extended innervation range. For example, in proportion to their body size, primates have larger forelimbs than rodents, yet spinal levels innervating forelimbs in these species are similar: C4–T2 in rats (Angélica-Almeida et al., 2013 and Takahashi and Nakajima, 1996) and C5–T1 in humans (Bromberg, 2014). The innervation of the bat forelimb extends beyond this range by six segmental levels. Moreover, focal injections demonstrated that a localized region of the wing can be innervated by DRG neurons distributed over 11 spinal levels. By contrast, small tracer applications in rodent limbs labeled neurons from three to six spinal levels (Bácskai et al., 2013 and Takahashi et al., 2003). We hypothesize that mid- and lower thoracic innervation in the bat derives from the trunk in development. During development, forelimb proprioceptors require motor neuron outgrowth to find their peripheral targets but cutaneous neurons do not (Swanson and Lewis, 1986). Thus, it is possible that the observed thoracic innervation in bat represents cutaneous neurons from the trunk that grow to reach local targets during development, whereas motor and proprioceptive neurons extend from upper thoracic levels (Bácskai et al., 2013, Ryan et al., 1997 and Tokita et al., 2012).

Our results also lend insight into the discontinuous organization of gracile and cuneate nuclei reported in Chiroptera (Martin, 1993). Unlike other mammals, somatotopic representations in brainstem nuclei of the flying fox do not preserve spatial relationships of peripheral tissues. Instead, representations of the body's surface are organized into bands that intermingle the trunk, plagiopatagium, hindlimb, and digits. Most notably, the back, abdomen, and side representations split the plagiopatagium representation into two parts. The observation that mid- and lower thoracic DRGs innervate all of these body sites suggests a peripheral basis for the unusual topography in bat gracile and cuneate nuclei. Future studies of brainstem nuclei in *E. fuscus* and other bat species are needed to evaluate this hypothesis and to determine whether organizational principles are conserved among flying mammals. Interestingly, thalamic and cortical regions are organized somatotopically in *E. fuscus* and other bats, although the forelimb representation is rotated compared with other mammals (Calford et al., 1985, Chadha et al., 2011 and Manger et al., 2001).

Along with neuronal specializations, wing evolution has resulted in unusual skin features. For example, Merkel cells were juxtaposed to almost half of wing hair follicles. By contrast, Merkel cells in the mouse coat selectively associate with guard hairs, which are the least prevalent hair type. We propose that the evolutionary loss of drag-inducing coat hairs on the bat wing can account for both the sparse distribution of wing hair follicles and high percentage associated with Merkel cells. Another unusual feature is that hair follicles appeared in all wing areas, including the ventral thumb, a region that is covered with glabrous skin in other mammals. Developmental studies of bat wings indicate that negative regulators of Bone Morphogenetic Protein (BMP) signaling during limb formation provide an anti-apoptotic signal that results in interdigital webbing (Weatherbee et al., 2006). In mice, inhibiting BMP signaling triggers ectopic hair growth on glabrous skin (Mayer et al., 2008); therefore, the anti-apoptotic mechanisms that govern wing membrane formation might also account for its unusual hair localization.

Hair-follicle receptors are proposed to serve as biosensors to detect changes in boundary-layer airflow and provide feedback to prevent stall (Dickinson, 2010 and Sterbing-D'Angelo et al., 2011). Detection of hair deflection is consistent with the function of lanceolate endings in other species, but our findings suggest an unconventional role in the context of flight: airflow sensing. In mice, different hair follicle types are innervated by distinct receptor complements; therefore, individual hairs serve as units of multi-modal tactile integration (Li et al., 2011). Similarly, we found that some hair follicles were associated with both lanceolate endings and Merkel cells. Interestingly, mouse hair receptors with overlapping receptive fields form columnar projections in the dorsal horn of the spinal cord (Abraira and Ginty, 2013). Defining the projections of wing tactile receptors and the circuitry by which they impinge on the motor system are important areas for future investigations.

The distribution of sensory endings across the wing indicates that tactile specializations could support distinct sensory-guided behaviors. For example, Merkel cells were concentrated on the phalanges, where they could provide information about surface features during climbing and food handling. This is consistent with their role in encoding object features in other mammals (Johnson et al., 2000). Based on the enrichment of diffuse endings in skin membranes, we propose that these receptors detect skin stretch and changes in wing camber. The identity of diffuse endings was not discernable from in vivo labeling; however, based on location and size, we hypothesize that they correspond to end-knobs observed in cryosections. The localization of end-knob receptors in hairy skin might be a specialization of the wing membrane, which is subjected to turbulent forces during flight (Muijres et al., 2008). DRG recordings are needed to confirm the functional identities of the bat wing's somatosensory receptors. Although the evolution of flight has proved to be an advantageous adaptation for Chiroptera, an open question is whether the wing's tactile receptors provide a selective advantage in flight. Chiroptera represents about 20% of all mammalian species, which provides rich material for comparing the behavioral consequences and functional organization of wing sensorimotor circuitry across species and ecological niches. Such future studies are needed to understand the evolutionary benefits of the bat wing's somatosensory specializations.

4. Neurophysiology

The wings of bats are equipped with a sparse grid of domed, microscopic hairs. The possible functional role of these wing hairs has been speculated since Cuvier mentioned them in the 1780s, and Sir Hiram Maxim proposed they could play a role in flight (Maxim 1912). Only recently have researchers begun to systematically study the anatomical and functional properties of these hairs and the tactile receptors that surround them (Marshall et al. 2015, Zook and Fowler 1986, Zook 2006). Previous histological and tracer studies revealed Merkel cells near hair follicles in two bat species (*Eptesicus fuscus*: Marshall et al. 2015, *Anthrozous pallidus*: Zook and Fowler 1986).

In the big brown bat, *Eptesicus fuscus,* about 50% of the wing hairs are associated with Merkel cell-neurite complexes. In addition, free nerve endings are present in the skin and lanceolate endings that surround follicles of *Eptesicus fuscus* wing hairs (Marshall et al. 2015). Removing tactile wing hairs with depilatory cream altered flight behavior in two bat species, *Carollia perspicillata* and *Eptesicus fuscus* (Sterbing-D'Angelo et al. 2011), which provides evidence that these hairs are functionally involved in flight behavior. In the present study, we characterized the functional role of tactile hairs of *Eptesicus fuscus* by stimulating the wing surface with calibrated air puffs and recorded single neuron responses in primary somatosensory cortex (S1) to varying air flow parameters, including magnitude, duration and direction.

Methods. Ten adult *Eptesicus fuscus,* weighing between 15 and 21 g, were used for electrophysiological recordings. *Electrophysiological recordings* - Extracellular, single-unit responses were acquired using a 16-channel linear electrode array connected via unity gain head-stage to a data acquisition system (Omniplex D System, Plexon Inc.). Neural signals were digitized at 16-bit resolution, sampled at 40 kHz, amplified 200-1000X, and band-pass filtered between 500-5000 Hz. Data acquisition was initiated via a dedicated PC terminal, and a TTL pulse was used to trigger and time-stamp the onset of stimulus delivery. Recordings were made from multiple electrode penetrations, spaced 100-250 μm apart from depths of 50-250 μm, ensuring that electrodes remained mostly within the supragranular layers of the cortex. Recording sessions lasted 4-6 hours, and each animal underwent 2-6 recording sessions spread over a period of 1-4 weeks. Spike waveforms and timestamps of extracellularly recorded potentials were extracted using commercially available software (Offline Sorter, Plexon Inc.). Single unit discrimination was achieved using manual amplitude thresholding and template matching. To further verify if the recorded waveforms belonged to single neurons, projections of the first two principal components were visualized as scatter plots for clustering. Finally, the presence of absolute refractory period in inter-spike interval histograms was used to declassify waveforms occurring with an interspike interval of less than 1ms. Further analysis on spike timestamps was done in Matlab (MathWorks Inc., version R2012a).

Tactile stimulation - With the electrode mounted to a micromanipulator, the contralateral wing was spread to full extension, and taped by the tip to a support frame, which was attached to the recording table. Subsequently, the electrode was advanced into the cortex and the wing and body surface stimulated using a set of calibrated monofilaments (von Frey hairs, North Coast). Von Frey hairs are available in sets of 20 with discrete, fixed weights. The hairs are calibrated in a logarithmic scale from 0.008 to 300 grams (0.08 – 2943 mN), within a 5% standard deviation. Stimulation consisted of pressing the monofilaments at right angles against the skin until they bent and subsequently released. Both dorsal and ventral wing surfaces were tested. Borders and center of receptive fields were determined, and cannula for air puff delivery placed close to the dorsal and ventral surface (3 mm distance), pointing at

25

the center of the tactile receptive field (RF). For stimulation with air puffs, a syringe with a 14 gauge blunt-tipped needle was directed at the RF center from different angles in 90 degree steps. Air puff stimuli were generated by a glue workstation (EFD Ultra®2400), and electronically varied in duration and amplitude. The air puff duration was varied between 40 and 1000 ms. Speed of airflow was measured using a hot-wire anemometer (Datametrics 100VT-A). For the range of intensities used in experiments, airflow speed varied between $3.3*10^{-2}$ to $2.5*10^{-1}$ m/s. We chose to limit the air flow magnitude to 0.25 m/s, because higher velocities indent the wing membrane and stimulate/recruit other receptor pools, e.g. stretch receptors. Since the airflow probe was placed 3 mm away from the wing surface, there was a time-delay for the air column to travel this distance. This time-delay was measured by recording the output of a MEMS microphone placed 3 mm from the stimulus probe, and was estimated to be ~ 30 ms. In reporting neuronal response latencies, this temporal offset was accounted for. At each recording site, the magnitude of the air puff was adjusted to be just above the neuronal response threshold, ensuring by microscopic inspection that no indentation of the membrane occurred. Each stimulus was presented 20 times, unless noted otherwise.

Results. To characterize the functional role of the wing hairs, extracellular single unit recordings were made from the primary somatosensory cortex (S1) of ten adult *Eptesicus fuscus.* First, the responses to varying airflow magnitude from 0.03 – 0.25 m/s were recorded. The duration of air puff stimuli was set to 40 ms (wing beat cycle: 35-45 ms); data from 35 well-isolated single units is presented here.

Spike count showed little change as a function of stimulus intensity above 0.9 m/s (R^2 range = $1.92*10^{-4}$ to 0.51, median R^2 = 0.11; slope range = -0.07 to 0.14, slope median = 0.04; Figure 4.1A). By contrast, onset latency decreased with airflow intensity and stabilized at higher stimulus levels, as revealed by a one parameter exponential model (R^2 range = 0.02 to 0.81, median R^2 = 0.49; decay constant range = –0.01 to -0.54, decay constant median = -0.04; Figure 4.1B).
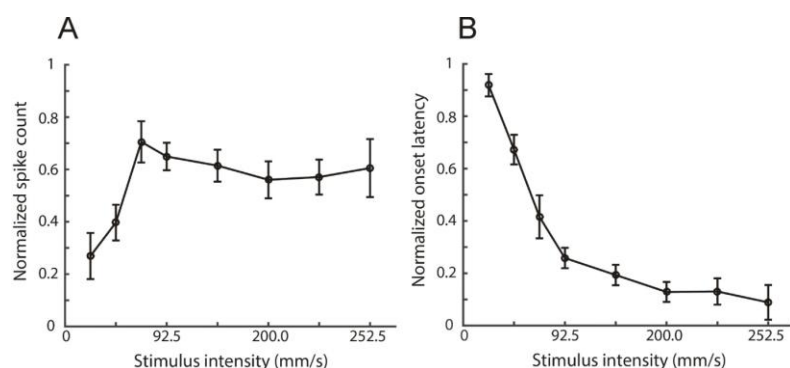

Figure 4.1: Neural population functions. A: Normalized stimulus intensity function (means and standard errors). The normalized spike count does not increase for air speeds above about 90 mm/s. B: Normalized first spike latency function (means and standard errors). Population averages were computed by linearly transforming the data from each neuron first (min-max normalization).

Secondly, we addressed the question whether single unit activity varies as a function of airflow duration and whether this relationship depends on the location of the receptive field on the wing membrane. Extracellular single neuron responses were recorded in S1 of four anesthetized *Eptesicus fuscus* in response to airflow stimuli of varying durations. Stimuli were delivered at, or just above threshold intensity (typically 1-2 psi = 0.03 m/s), while the duration was varied from 10 ms to 1 s. Figure 4.2 shows spike raster plots, peri-stimulus time histograms for three example neurons with receptive fields centered on different parts of the wing.
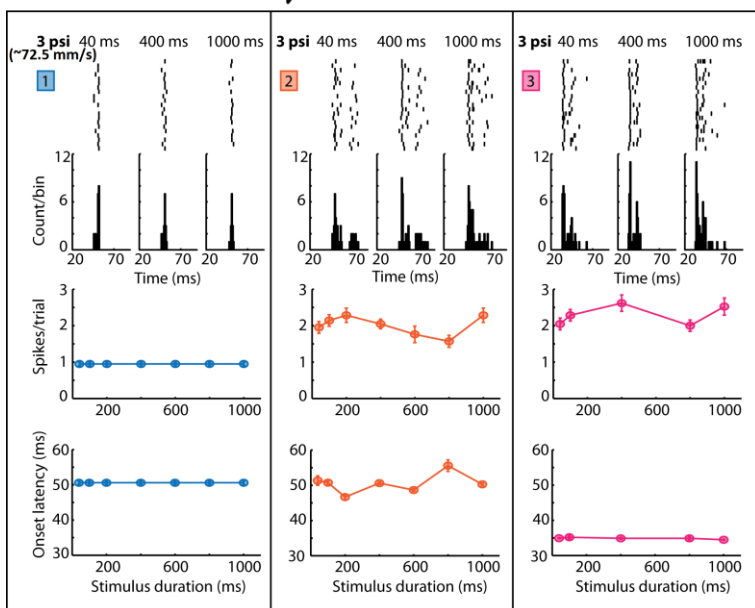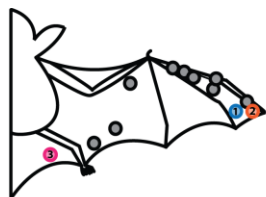
The individual neurons showed little response variation to airflow duration (linear regression of spike count: R^2 range = 0.001 to 0.212, median R^2 = 0.04; slope range 0 to 0.0013, slope median = 0. Linear regression of onset latency: R^2 range = 0 to 0.35, median R^2 = 0.06; slope range = -0.002 to 0.011, slope median = 0.002). The same was true for the population average.

Figure 4.2: Cortical responses to varying airflow stimulus duration. On the top is a schematic of a bat with the location of sampled receptive field (circles). Below are raster plots, post-stimulus time histograms, mean spikes/ trials and mean onset latencies of three representative neurons. Receptive field locations of these neurons are color matched to the circles in the bat schematic.
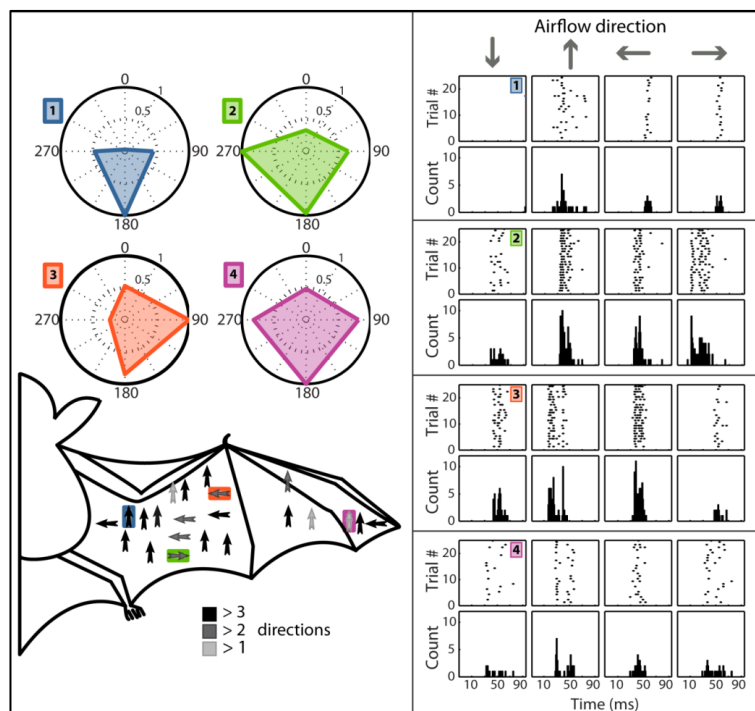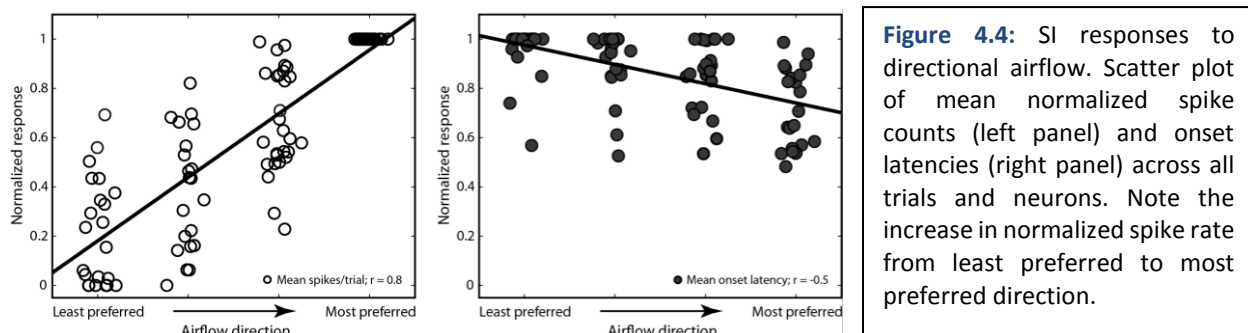

Figure 4.3: Directional selectivity of SI neurons to airflow stimulation. Polar plots, spike rasters, and post-stimulus time histograms showing response of four representative neurons (spike counts normalized to the maximum) to near threshold airflow stimuli delivered from four directions. Receptive field locations of these units are color matched to arrows in the bat schematic. The preferred direction is denoted by arrows in the bat schematic, with arrow shades indicating the strength of selectivity, i.e., black, dark gray, and light gray correspond to significantly higher firing compared to remaining three, two or one directions respectively.

Twenty-two well-isolated single S1 neurons from four bats were acquired in response to airflow stimuli delivered from four directions (90° steps, rostro-caudal and medio-lateral axes). Response to stimulation (mean spikes/trial) for the preferred direction was compared to the remaining stimulus directions by one-way analysis of variance (ANOVA)

Figure 4.4: SI responses to directional airflow. Scatter plot of mean normalized spike counts (left panel) and onset latencies (right panel) across all trials and neurons. Note the increase in normalized spike rate from least preferred to most preferred direction.

Third, extracellular spike waveforms of and Bonferroni's post-hoc test. In agreement with the previously reported multi-unit results (Sterbing-D'Angelo et al. 2011), all sampled single neurons showed directional selectivity (Figure 4.3, direction of arrows in the bat schematic), with a majority strongly selective for a single direction (i.e., significantly higher firing compared to all remaining stimulus directions; 14/ 22, or 64% of the units). Furthermore, a majority (15/22 or 68%) of neurons were tuned to reverse airflow direction.

The number of spikes elicited in response to airflow stimulation varied as a function of direction, as reported above. The airflow response curves thus provided an estimate of directional selectivity exhibited by S1 neurons. Response latency was analyzed across all stimulus directions, as spike timing could potentially carry information about airflow characteristics. However, calculating the Fano factor of the spike time data did not yield a statistically relevant result. In contrast to flow velocity and flow duration, there is a clear spike rate code for flow direction. For the population of sampled neurons, response latency varied as a function of airflow direction and not surprisingly, the stimulus direction evoking the highest firing rate (preferred direction) also showed the shortest response latency (Figure 4.4).

Discussion. *Airflow responses in bat S1-* Our electrophysiological recordings from supragranular primary somatosensory cortex of the big brown bat, *Eptesicus fuscus*, reveal that tactile information produced by spatially restricted (<1 cm^2) air puff stimulation of the wing surface reaches the cortex as a sparse, temporal, "onset-only" code, with little change in spike counts as a function of stimulus intensity above close-to-threshold airflow velocity. Hence, we hypothesize that the wing hairs sense changes in airflow, and not air speed.

The airflow pattern across a bat's wing during flapping flight is complex rather than sinusoidal, which has been used to classify arthropod tactile hair responses (Humphrey et al. 2003). Flapping of bat wings generates airflow with high-frequency components in the range caused by vorticity. Big brown bats fly at speeds ranging from 3 to 9 m/s, flapping their wings at a rate of 11-15 Hz (Kurta and Baker 1990), with the two parameters interdependent, at least at low flight speeds (Bullen and McKenzie 2002). At typical wing beat rates, each stroke (up or down) lasts approximately 35-45 ms. Hence we chose an air flow duration of 40 ms for our experiments. Together, flight speed and wing beat frequency, along with other kinematic parameters, shape the resulting airflow patterns across the wing (Hedenström et al. 2007).

While there are no particle image velocimetry (PIV) data available for *Eptesicus fuscus*, PIV measurements from a similarly sized, but slow flying (1 m/s) bat species (*Glossophaga soricina*) indicated that the area of reversed air flow caused by the leading edge vortex can stretch up to 3 cm cord-wise, almost covering the entire rostro-caudal wing surface (Muijres et al. 2008).

Our data indicate that spike timing might play a role in the representation of complex airflow patterns across the bat wing. S1 activity in response to airflow stimulation is generally rapidly-adapting, which is not surprising given the abundance of lanceolate receptors at the wing hairs follicles. However, the quite substantial presence of Merkel cell neurite complexes in the wing membrane (Marshall et al. 2015), which are traditionally considered slowly-adapting (SA) receptor structures, would suggest that we should find also SA responses. This is not the case. One explanation would be that it has been suggested that the SA characteristic of Merkel cell afferents might be the result of a population code carried by large clusters of Merkel cells (e.g., GüÇlü et al. 2008). Moreover, it is known that the sustained portion of the Merkel-cell afferent response in mice results from the contributions of many Merkel cells (Maksimovic et al. 2014). Often, we found only one or two Merkel cells associated with the wing hairs. Such a small number might not be sufficient to create a SA response based on a population code.

The traditional view has been that the SA and RA characteristic of touch information ascending to cortex remains segregated into sub-modalities in the dorsal column nuclei of several mammalian species (Douglas et al. 1978, Vickery et al. 1994) and the somatosensory thalamus (Herron and Dykes 1986). However, recent evidence suggests that convergence of tactile sub-modalities occurs earlier in the somatosensory pathway. Using tracer techniques, Sakurai et al. (2013), found both RA and SA neurons of the mouse vibrissae follicle marked at the level of brainstem, thalamus, and cortex. They reported anatomical convergence of RA and SA projections at all these levels. Pei et al. (2009) found neurons whose response to a step indentation was similar to either an SA or an RA afferent. However, approximately 50% of the S1 neurons they studied responded to a step indentation with both a sustained response and a transient off response, suggesting that these neurons received convergent input originating from both SA and RA afferents. Convergence would also explain the RA responses predominantly found in the present study.

Another question is whether the directionality of the wing hair responses is created by the ascending projection pattern, at the primary afferents, the receptor structures at the follicle, and/or the hair itself (angle, curvature). Our SEM analysis showed that the cross-section of the hairs is circular, but the orientation and angle (re. membrane) of the hairs is not preserved during the tissue processing necessary for SEM. Hence, we cannot exclude any of these factors. Rutlin et al. (2014) presented evidence that a subset of mouse lanceolate afferents display directional selectivity that is the result of their polarized morphology on one side of the hair. We observe both polarized lanceolate endings that localize to one side of hairs (Marshall et al., 2015), and non-polarized lanceolate endings that encircled bat wing hairs. This leaves open the possibility that directional selectivity could arise at some primary afferent terminals.

Invertebrates - Hair-like flow sensing structures have been reported in species across many orders in the animal kingdom, including moth olfaction (Koehl et al., 2001) and fluid sensing in arthropods in air and water (Barth et al., 1993; Devarakonda et al., 1996; Humphrey et al., 2003). Airflow sensing using filiform hairs partially or fully immersed in the boundary layer around the body has been extensively studied in arthropods, particularly in spiders and crickets (Shimozawa and Kanou, 1984; Barth et al., 1993), and these sensors exhibit an exquisite sensitivity close to thermal noise level (Shimozawa et al., 2003). The neuronal

thresholds found in the present study are significantly higher, which is not surprising, because the bat wing hairs have a different function than the arthropod sensors. The arthropod sensors detect the finest variation in the flow field associated with the movement of prey, while the wing hairs monitor vorticity around the wing membrane during rapid flapping flight. Like in the spider and cricket, the bat wing hairs are presumably fully immersed in the boundary layer (Dickinson 2010).

Variation of hair length is assumed to allow spiders and crickets to extract the intensity and frequency range of the airflow stimulus. The cephalic trichoid sensilla of locusts, e.g., Schistocerca species, range in length from 30 to >250 µm (Smola 1970). These sensors also show directional sensitivity. Experiments isolating different components of the system show that this directional response is a result of angular deflection of the shaft, which is a function of direction and speed of airflow, as well as mechanical and physiological properties of the system itself. Knowing the directional tuning of individual sensilla, the directional properties of the entire fields have been mapped (Taylor and Krapp 2007). As described above, we cannot exclude that the orientation and curvature of the hairs are involved in creating directional sensitivity we observed in bat S1 neurons. However, the asymmetrical distribution of Merkel cells around the hair follicle suggests that the receptor base could very well create directionality independent of the hair geometry. Also, as described above, polarized LTMR lanceolate endings create directionality as well.

Birds - In birds, mechanoreceptors at the base of specialized hair-like feathers have been described. There are four main types distinguished: Herbst corpuscles (HC), Merkel cell receptors, Grandry corpuscles and Ruffini endings. Necker (1985) and Hörster (1990) have characterized the response properties of Herbst corpuscles and suggested their role in flight control. Herbst corpuscles are the most widely distributed receptors in bird skin. To address the role of wing associated mechanoreceptors in flight control, Brown and Fedde (1993) recorded activity from radial nerve of a chicken while either manually moving the alular joint and leading edge feathers, or using airflow stimuli delivered through a tube. They noted that discharge frequency increased with elevation of covert (contour) feathers or extension of the alular joint. Elevation of covert feathers increased with angle of attack up to 40 deg, beyond which stall (separation of flow) occurs. In addition, an increase in velocity of airflow led to increased firing rate of the secondary feather-filoplume receptors, thought to be vibrotactile Herbst corpuscles. This led the authors to conclude that wing associated mechanoreceptors could detect possible stall at high angles of attack. Similarly, the bat's wing hairs could send signals to the CNS about stall at high angles of attack, which predominantly occur during slow flight, particularly while the animal is hovering and banking. During such flight maneuvers extensive leading-edge vortices have been observed (Muijres et al. 2008). It should be emphasized, though, that the bat wing hairs are much smaller and shorter (< 1mm) than bird feathers and filoplumes. They most likely do not sense airflow beyond the boundary layer of the wing.

In summary, we conclude that the sparse and precisely timed responses with RA characteristics we observed in S1 are well suited to detect sudden changes in airflow, and the preference for reverse airflow suggests that S1 neurons of the bat serve as stall detectors rather than long-term airspeed monitors. Through evolutionary adaptations, bats have developed specialized sensorineural mechanisms to increase the robustness and maneuverability of their flight, even in the most adverse situations. Our study of the bat somatosensory system suggests that a sparse code mainly based on spike rate may operate to detect the fast changes in airflow patterns, which is needed to sustain flight at the high wing beat rates of the bat.

5. Biomimetic air flow sensor

From the scanning electron microscopy results and the laser scanning vibrometry tests we developed a concept for a representative, biomimetic "air flow hair" design (Figure 5.1). The prototype has high sensitivity due to diaphragm that provides capacitance amplification, and is characterized by a simple, robust mechanical structure that can withstand the mechanical challenges of flapping flight.
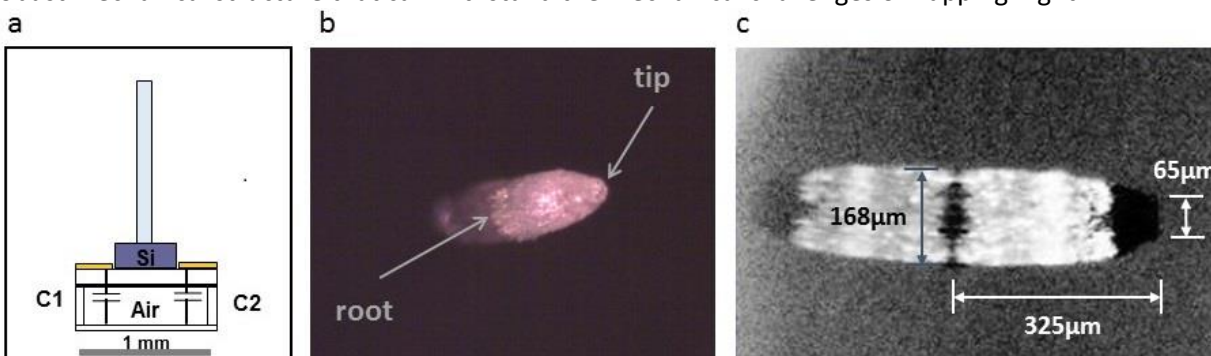

Figure 5.1. Biomimetic air-flow sensor. a) Overall design of the sensor. Air cavity diameter: 1000µm, air cavity height: 15µm, gold electrode thickness: 100nm, Polymer diaphragm thickness: 5µm, Hair length: 1000µm, Silicon mesa diameter: 200µm, Size of air volume: 5.1x5.1x5.25mm. b) Microphotograph of the manufactured hair. The arrows point to the root and the tip of the structure. C) Side view of the hair with dimensions indicated by the bars.

For prototyping we chose the material Ormocomp, which has bending properties similar to the bat's tactile wing hairs (E = 1.6 GPa, ρ = 1.2x103 kg/m3, ν =0.35), see Figure 5.2. The designed hair has a natural frequency of 32.3 kHz, which is also in the mean range of the biological hairs. It is designed for airflow velocities between 1-3 m/s, which matches the range of the bats' flight speed under experimental conditions in our flight rooms at Johns Hopkins University.
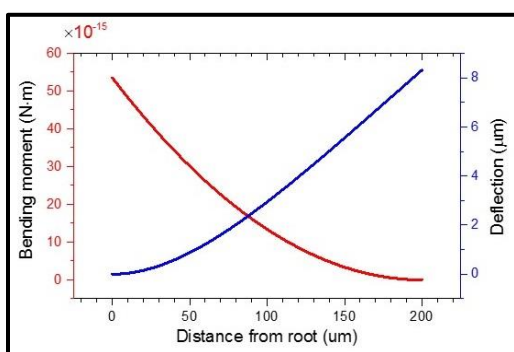

Figure 5.2. Bending characteristics of our biomimetic air-flow sensor. Bending moment (left y axis) and absolute deflection (right y axis) of the artificial hair as functions of the distance from root. The deflection properties match the properties of the biological hair as previously measured using contact-free laser scanning vibrometry.

The bat's wing hairs are highly directional. Most of them have been shown to prefer reverse air flow (Sterbing-D'Angelo et al. 2011). Hence, we designed the biomimetic air flow sensor to sense the direction of the air flow by implementing four electrodes (Figure 5.3). The differential capacitance is 225 aF at the lowest modelled air flow velocity (0.5 m/s) which would be sufficient to pick up even the slowest air speeds that our bats can produce.
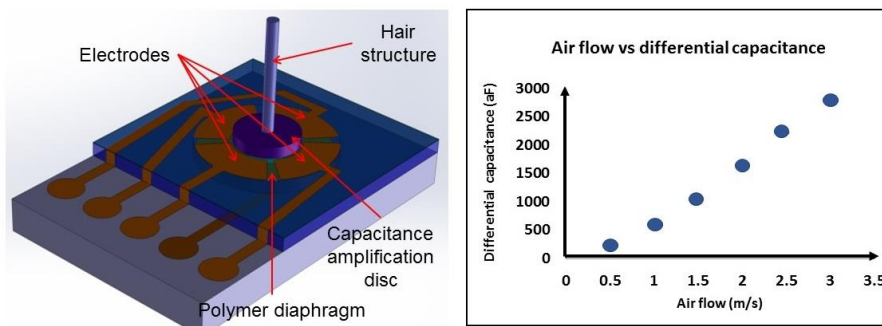
31

Figure 5.3. Directional design of our biomimetic air-flow sensor. Left: Note the four electrode structures on opposite sides of the cantilever "hair". Right: The average flight speed of the Big Brown Bat is 2.5 to 3 m/s in our flight room facility. The differential capacitances of our sensor design allows differential capacitance readouts of up to 3000 aF at the highest modeled air flow velocities.

The sensing mechanism is based on measure coupling between electrodes on membrane and substrate as the "hair" deflects due to airflow (capacitive coupling and differential detection). Our finite element model predicts that the signal will range from 100 aF at 0.5 m/s to 30 fF at 3 m/s. This will allow the device to operate in an environment comparable to the flight environment of the bat.

6. Functional role of the nose leaf and facial vibrissae in *Carollia perspicillata*

The neotropical bats of the family Phyllostomidae (Leafnosed Bats) are characterized by a "noseleaf" that aids in directing the echolocation beam, which is emitted through the nostrils of these bats. The bats move the noseleaf actively during sound emission. It was thought that the function of the noseleaf is primarily to shape the sonar beam in the vertical axis, but our preliminary high-speed video revealed that the noseleaf can also be rotated horizontally. In addition, it became evident that the noseleaf touches an array of vibrissae that are protruding from domes behind the noseleaf (Figure 6.1 c). The functional role of the domed vibrissae behind the noseleaf is unknown. We hypothesize that they provide the echolocating animal with a re-afference signal of the exact noseleaf position that enables the bat to segregate echoes. This information would be particularly valuable in cluttered environments and/or multi-bat foraging situations where the bats have to distinguish between their "own" echoes and the echoes produced by other bats.
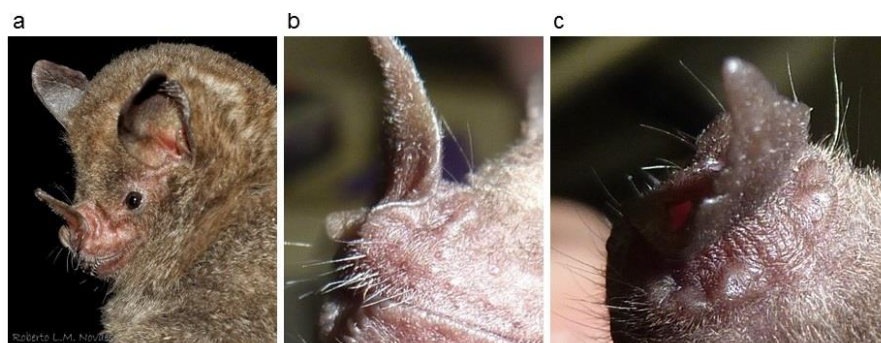

Figure 6.1. a) Portrait of a Short-tailed fruit bat (*Carollia perspicillata*), a frugi-nectarivorous laryn-geal echolocator of the neotropics. b) Side view of the nose and mouth area. Note the vibrissae located caudally from the noseleaf. c) Top view of the nose. The vibrissae are protruding from an organized row of domes. There are 3 major hairs on each side.

Our first approach was to find and map the primary somatosensory cortex (S1) of this species, find the cortical region devoted to the nose area, and deflect the noseleaf under controlled experimental conditions, so that the vibrissae behind it are deflected. We also injected fluorescent tracers into the vibrissal domes to characterize the tactile receptors within the domes (Figure 6.2a).
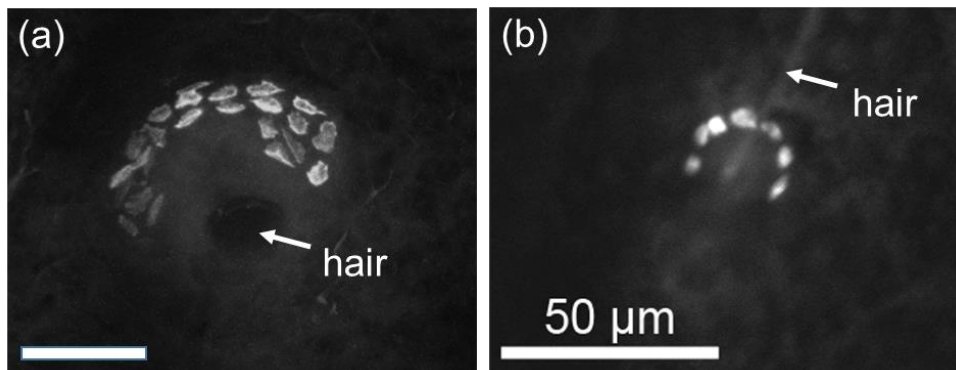

Figure 6.2. Merkel cells. a) Merkel cells marked by the specific antibody K20 attached to a fluorescent tracer. The arrow points to the actual hair (vibrissa) at the center of the dome. The Merkel cells are arranged in form of a multi-row patch, very similar to Merkel cells found around mouse whiskers (K. Marshall, pers. comm.). b) Merkel cells around an air-flow sensing hair on the bat wing. On the wing the Merkel cells are arranged in a small, single-file ring around microscopically small hairs (Marshall et al. 2015).

The primary somatosensory cortex of *Carollia perspicillata* is located on the medio-rostral surface of each cortical hemisphere. Systematic mapping revealed a similar organization of neighboring body parts as previously described for other bat species, e.g., the Big Brown Bat (Chadha et al. 2010), with the lower extremity and the back represented medially and the upper extremity (wing) and head represented more laterally (Figure 6.3).

Electrophysiological recordings - Extracellular, single-unit responses were acquired using a 16-channel linear electrode array connected via unity gain head-stage to a data acquisition system (Omniplex D System, Plexon Inc.). Neural signals were digitized at 16-bit resolution, sampled at 40 kHz, amplified 200-1000X, and band-pass filtered between 500-5000 Hz. Data acquisition was initiated via a dedicated PC terminal, and a TTL pulse was used to trigger and time-stamp the onset of stimulus delivery. Recordings were made from multiple electrode penetrations, spaced 100-250 μm apart from depths of 50-250 μm, ensuring that electrodes remained mostly within the supragranular layers of the cortex. Recording sessions lasted 4-6 hours, and each animal (N=2) underwent 2-6 recording sessions spread over a period of 1-4 weeks. Spike waveforms and timestamps of extracellularly recorded potentials were extracted using commercially available software (Offline Sorter, Plexon Inc.). Single unit discrimination was achieved using manual amplitude thresholding and template matching. To further verify if the recorded waveforms belonged to single neurons, projections of the first two principal components were visualized as scatter plots for clustering. Finally, the presence of absolute refractory period in inter-spike interval histograms was used to declassify waveforms occurring with an inter-spike interval of less than 1ms. Further analysis on spike timestamps was done in Matlab (MathWorks Inc., version R2012a).
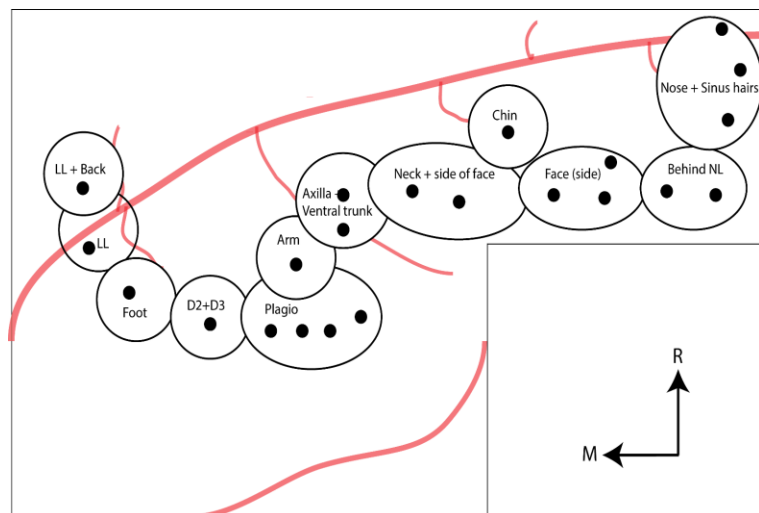
Figure 6.3. Cortical map. Moving the electrode systematically from medial to lateral revealed an orderly representation of the bat's body surface with the face and nose represented most rostro-laterally.

Tactile stimulation - The electrode was advanced into the cortex and the body surface stimulated using a set of calibrated monofilaments (von Frey hairs, North Coast). Von Frey hairs are available in sets of 20 with discrete, fixed weights. The hairs are calibrated in a logarithmic scale from 0.008 to 300 g (0.08 – 2943 mN), within a 5% standard deviation. Stimulation consisted of pressing the monofilaments at right angles against the skin until they bent and subsequently released. Borders and center of receptive fields were determined, and cannula for air puff delivery placed close to the noseleaf or vibrissal dome (3 mm distance), pointing at the center of the tactile receptive field (RF).

For stimulation with air puffs a syringe with a 14 gauge blunt-tipped needle was directed at the RF center. Air puff stimuli were generated by a glue workstation (EFD Ultra®2400), and electronically varied in duration and amplitude. The air puff duration was varied from 50 to 1000 ms. The speed of airflow was measured using a hot-wire anemometer (Datametrics 100VT-A). For the range of intensities used in experiments, airflow speed varied between $3.3*10^{-2}$ to $2.5*10^{-1}$ m/s. Since the airflow probe was placed 3 mm away from the skin, there was a time-delay for the air column to travel this distance. This time-delay was measured by recording the output of a MEMS microphone placed 3 mm from the stimulus probe, and was estimated to be ~ 30 ms. In reporting neuronal response latencies, this temporal offset was accounted for.

The preliminary experiments revealed that the receptive fields on the noseleaf and the vibrissal domes are extremely small compared to other body regions, indication high sensitivity and high spatial discrimination of tactile features. For RFs located on the domes, the air puffs were directed at the frontal noseleaf. The noseleaf was bent caudally by the puff and deflected the vibrissae. Figure 6.4 shows examples of single neuron recordings made before and after the removal of the vibrissa centered in the receptive field (red circle). The data indicates, that the receptors in the vibrissal dome are indeed activated by the deflection of the nose leaf, and that the cortical neuronal response seizes when the hair is removed.

Figure 6.4. Single neuron responses before/after removal of the vibrissa. Left: the red circle indicates the size and location of the neuronal receptive field. Only stimulation of this one dome elicited a cortical response. Right: Spike raster plots and peri-stimulus time histograms of 2 single neurons with RFs in the same location before (left column) and after (right column) hair removal.
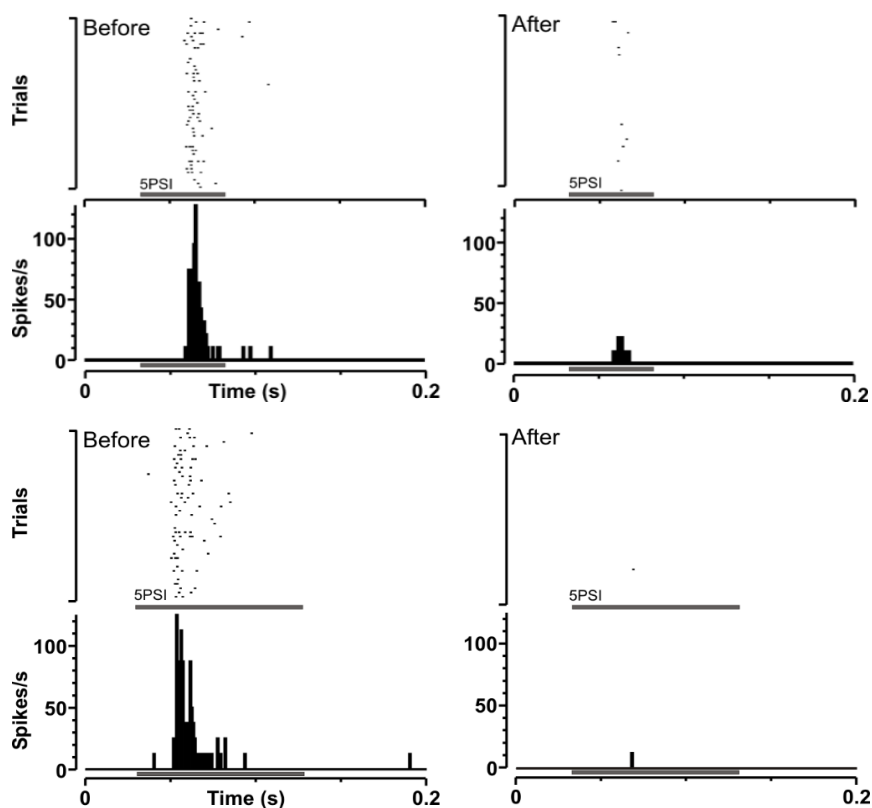
7. Important next steps that justify renewed support

Discovering the cortical encoding of airflow across the bat wing poses two key challenges: (1) how to determine the aerodynamic forces experienced by individual hairs (which have a scale of ~ 100 microns) on a bat wing in natural flight; and (2) how to decode the processing of this sensory information in the brain of the animal and the subsequent feedback control that it generates in response to these signals. We propose to overcome these challenges using an innovative research approach that integrates state-of-the-art experimental (fluorescent micro-PIV) and computational flow modeling with neurophysiological assays and neurosensory modeling. The objective of this proposed research is to develop and test a first-of-its-kind experimental apparatus which, together with computational flow and neurosensory feedback modeling, will enable measurement of sensory responses of bat wings to realistic flow patterns. We hypothesize that bat wing hairs, not exceeding the boundary layer, carry information about airflow separation to the central nervous system. We further hypothesize that the animal employs neurosensory feedback to guide wing adjustments to optimize lift and prevent stall. Since stall detection is a crucial and so far unresolved aspect for stabilization of flight of unmanned micro-air vehicles, as well as for large-scale commercial airplanes, the proposed research will yield important new data and can lead to innovative solutions for flight control.

35

8. Relevance of this research to AFOSR

Understanding the mechanisms biological neural systems employ for the stabilization of flight under adverse conditions (wind gusts, group flight) is of tremendous importance for the designs of novel air crafts, e.g., autonomous flying platforms. Distributed air flow and stall sensor systems, as we have discovered in the bat, are an important factor for the development of biomimetic solutions to improve robustness and maneuverability of flight.

II. Publications, presentations, and press links 2012-2017

Sterbing, S.J., Moss, C.F. (in print) Comparative analysis of the distribution and morphology of tactile hairs on the wing membrane of four bat species. *Journal of Mammalogy*.

Sterbing-D'Angelo, S.J., Chadha, M., Marshall, K.L. and Moss, C.F., 2016. Functional role of airflow sensing hairs on the bat wing. *Journal of Neurophysiology*, pp.jn-00261.

Sterbing-D'Angelo, S.J., Liu, H., Yu, M. and Moss, C.F., 2016. Morphology and deflection properties of bat wing sensory hairs: scanning electron microscopy, laser scanning vibrometry, and mechanics model. *Bioinspiration & Biomimetics*, *11*(5), p.056008.

Sterbing-D'Angelo, S. and Moss, C.F. (in press) Evolution of flight and echolocation in bats. In J.Kaas and S. Herculano-Houzel (Eds), *Evolution of Nervous Systems*, Second Edition, Elsevier, Amsterdam.

Marshall, K., Chadha, M., DeSouza, L., Sterbing-D'Angelo, S., Moss, C.F. and Lumpkin, E.A., 2015. Bats have evolved unique sensory circuitry that supports mammalian flight. *Cell Reports*, 11, 851–858.

Falk, B., Kasnadi, J. and Moss, C.F., 2015. Tight coordination of aerial flight maneuvers and sonar call production in insectivorous bats. *Journal of Experimental Biology*, *218*(22), pp.3678-3688.

Falk, B., Jakobsen, L., Surlykke, A. and Moss, C.F. Bats coordinate sonar and flight behavior as they forage in open and cluttered environments, *Journal of Experimental Biology*, 2014 217:4356-4364.

Sterbing-D'Angelo, S.J. and Moss, C.F., 2014. Air flow sensing in bats. In *Flow Sensing in Air and Water* (pp. 197-213). Springer Berlin Heidelberg.

Presentations (selected)

Sterbing-D'Angelo, S.J. Wired for flight: the role of tactile sensing for flight control in bats. Office of Assistant Secretary of Defense for Research and Engineering Basic Research Forum, Arlington VA, 2015. Invited.

Sterbing-D'Angelo, S., Chadha, M., Liu, H., Yu, M., Marshall, K., Lumpkin, E.A. and Moss, C.F., 2015. Functional role of tactile hairs on the bat wing. In: *"Mammalian Circuits Underlying Somatosensation"*, Howard Hughes Medical Institute, Janelia Research Campus, Nov.15-18. Invited.

Chadha, M., Marshall, K.L., Sterbing-D'Angelo, S.J., Lumpkin, E.A. and Moss, C.F., 2012. Tactile sensing along the wing of the echolocating bat. Eptesicus fuscus. In *Soc Neurosci Abstr* (Vol. 523, No. 03).

Press Links (selected)

http://www.forbes.com/sites/hilarybrueck/2015/05/14/learning-to-fly-why-planes-and-drones-could-take-their-next-cue-from-bats/

http://time.com/3841849/bats-flight-air-travel/

http://www.nbcnews.com/science/science-news/tiny-hairs-bats-wings-key-their-maneuverability-n352161

http://news.discovery.com/animals/bat-wing-super-sensorsguide-acrobatic-flight-150430.htm

http://www.wired.com/2015/04/bat-flight/

http://news.sciencemag.org/plants-animals/2015/04/sense-touch-turns-bats-acrobats

http://www.dailymail.co.uk/sciencetech/article-3062468/Holy-agility-Batman-Touch-sensors-tips-wings-bats-precise-flying-skills.html?ITO=1490&ns_mchannel=rss&ns_campaign=1490

https://www.washingtonpost.com/news/speaking-of-science/wp/2015/04/30/bats-use-a-super-sense-of-touch-to-fly-with-precision/

http://www.sci-news.com/biology/science-bats-touch-sensors-02753.html

http://www.thestar.com/news/world/2015/04/30/can-bats-teach-aircraft-designers-a-thing-or-two.html

http://www.techtimes.com/articles/49922/20150430/bat-wings-tiny-hairs-hold-secret-remarkable-

http://news.yahoo.com/bat-wings-harbor-special-sensory-cells-112532417.html

http://neurosciencenews.com/bat-flight-touch-evolution-2016/

http://phys.org/news/2015-04-keen-nimble-flight.html

https://www.newscientist.com/article/dn27449-bats-use-unusual-touch-sensors-to-catch-a-mid-air-meal/
        *New Scientist picture of the day on April 30th

http://www.innovations-report.com/html/reports/life-sciences/touch-sensors-on-bat-wings-guide-flight.html

http://www.futurity.org/wings-bats-flight-914792/

*The Scientist Image of the day on May 4th, 2015:

http://www.the-scientist.com/?articles.view/articleNo/42876/title/Image-of-the-Day--Bat-Brains/

III. Personnel and Collaborators

Susanne J. Sterbing-D'Angelo, Ph.D.

Cynthia F. Moss, Ph.D.

Wei Xian, M.S.

Silvio Macias, Ph.D.

Mohit Chadha, Ph.D.

Benjamin Falk, Ph.D.

Dan Ju, undergraduate honors student

Grant Shewmaker, undergraduate honors student

Collaborators:

Ellen Lumpkin, Kara Marshall (Columbia University)

Miao Yu, Haijun Liu, Pamela Abshire, Timothy Horiuchi, Nuno Martinez (University of Maryland)

IV. References

Abraira E, Ginty D, *Neuron* **79** 618–39 (2013).
Ackert JE, *J Morphol* **25** 301–34 (1913).
Adineh VR, *et al. Acta Biomater.* **21** 132–41 (2015).
Ai H, *et al., J Insect Physiol* **56** 236–46 (2010).
Albert J, *et al., J. Comp. Physiol.* A **187** 303–12 (2001).
Andermann ML*, et al., Neuron* **42** 451–64 (2004).
Angélica-Almeida M, *et al. Acta Med Port* **26**: 243–250 (2013).
Augurelle AS, *et al.*, *J Neurophysiol* **89**: 665–671 (2003).
Azim E, *et al. Nature* **508**: 357–363 (2014).
Bácskai T, *et al., Brain Struct Funct* **218**: 221–238 (2013).
Barth FG, *et al.*, *Phil. Trans. Royal Soc Lond B: Biol Sci* **340**, 445-61 (1993).
Basbaum AI, *et al., Cell* **139:** 267–284 (2009).
Bathellier B, *et al., J Comp Physiol* A **191** 733–46 (2005).
Bromberg MB, *Neuron* **78**: 191–204 (2013).
Brown RE, Fedde MR, *J Exp Biol* **179**: 13-30 (1993).
Budick SA, et al., *J Exp Biol* **210** 4092–103 (2007).
Bui TV, et al., *Nature* **313**: 477–479 (1985).
Bullen RD, McKenzie NL, *J Exp Biol* **205**: 2615-2626 (2002).
Bullen RD, McKenzie NL, *Austral J Zool* **56**: 281–296 (2008).
Burkhardt D, Gewecke M, *Cold Spring Harb Symp Quant Biol* **30** 601–14 (1965).
Calford MB*, et al., Nature* **313**: 477–479 (1985).
Camhi JM. *J Exp Biol* **50**: 349-362 (1969).
Chadha M*, et al.*, *J Comp Physiol A* **197**: 89–96 (2011).
Cheney JA, *et al., Bioinspir Biomim* **9:** 025007 (2014).
Chickering JG, Sokoloff AJ, *Brain Behav Evol* 47: 1–7 (1996).
Cretekos CJ, *et al. Dev Dyn* **233**: 721–738, 2005.
Debelica A, Thies ML, In Special publications of the Museum of Texas Tech University, (RJ Baker, series ed), Museum of Texas Tech University Press (2009).
Dechant HE, *et al., J Comp Physiol A* **187**: 313–22 (2001).
Devarakonda R, *et al., Philos Trans R Soc Lond B Biol Sci* **351**,933 -946 (1996).
Dickinson MH, *J Exp Biol* **151** 245–61 (1990).
Dickinson BT., *Bioinspir Biomim* **16**:016002, (2010).
Douglas PR, *et al., J Physiol* **285**:493-513 (1978).
Esposito MS, *Nature*. 2014; 508: 351–356
Falk B*, et al.*, *J Exp Biol* **218** 3678–88 (2015).
Farney J, Fleharty ED*, J Mammal* **50**: 362-367 (1969).
Florence SL, et al., *J. Comp. Neurol.* 1989; 286: 48–70

Fuller SB, *et al., Proc Natl Acad Sci* **111** E1182–91 (2014).

Gao N, *et al., Sci. Rep.* **6** 19935 (2016).

Gewecke M, Schlegel P, *J Comp Physiol* A **67** 325–62 (1970).

Gewecke M, Woike M, *Z Tierpsychol* **47** 293–8 (1978).

GüÇlü B, *et al., Somatosens Motor Res* **25**: 123-138 (2008).

Haake AR, *et al., Dev Biol* **106** 406–13 (1984).

Hartmann MJ, *et al., J Neurosci* **23** 6510–9 (2003).

Hayward B, Davis R, *J Mammal* **45**: 236-242 (1964).

Hedenström A, *et al., Science* **316**: 894-897 (2007).

Herron PA, Dykes RO., *J Neurophysiol* **56**:1475-97 (1986).

Hinterwirth AJ, Daniel TL, *J Comp Physiol* A **196** 947–56 (2010).

Horowitz SS, et al., *J. Vestib. Res.* 2004; 14: 17–32

Hörster W., *J Comp Physiol A* **166**: 663-673 (1990).

Hubel TY, et al., *J. Exp. Biol.* 2010; 213: 3427–3440

Humphrey, JAC, *et al.* In *Ecology of Sensing* (ed. F.G. Barth, A. Schmid), pp.105 -115. Springer (2010).

Iggo A, Muir AR, *J. Physiol.* 1969; 200: 763–796

Jadhav SP, et al., *Nat. Neurosci.* 2009; 12: 792–800

Johnson KO, *et al., J. Clin. Neurophysiol.* **17** 539–58 (2000).

Johnson KO, *Curr Opin Neurobiol* **11** 455–61 (2001).

Kan Q, *et al., Mater Res Bull* **48** 5026–32 (2013).

Kandel ER, et al. Principles of Neural Science, Fifth Edition. McGraw-Hill, ; 2012

Khan I, *et al., BMC Genomics* **15** 779 (2014).

Klopsch C, *et al., J R Soc Interface* **10** 20120820 (2013).

Koehl MA, *et al., Science* **294**:1948-51 (2001).

Kurta A, Baker RH, *Mammal Spec* **356**: 1-10 (1990).

Landmesser LT, *Int. J. Dev. Neurosci.* 2001;19: 175–182

Lawlor TE, *J Mammal* **54**: 71–78 (1973).

Lesniak DR, et al. *eLife*. 2014; 3: e01488

Lewin GC, Hallam JA, *J Comp Physiol* A **196**: 385–95 (2010).

Li L, et al., *Cell*. 2011; 147: 1615–1627

Makanya AN, et al., *J. Anat.* 2007; 211: 687–697

Maksimovic S, *et al., Nature*, **509** (7502), 617-21 (2014).

Mamiya A, et al., *J Neurosci* **31** 6900–14 (2011).

Manger PR, et al., *Somatosens. Mot. Res.* 2001;18: 19–30

Marshall K, *et al., Cell Reports* **11**, 851–858 (2015).

Martin RL, et al., *J. Comp. Neurol.* 1993; 335: 334–342

Maxim H., *Sci Am* **27**: 80-81 (1912).

Mayer JA, et al., *Am J Pathol* **173**: 1339-1348 (2008).

Meyers JR, et al. *J. Neurosci.* 2003; 23: 4054–4065

Muijres FT, *et al., Science* **319**:1250-1253 (2008).

Muijres FT, *et al., Bioinsp Biomim* **9**(2):025006 (2014).

Munger BL, Ide C, *Arch. Histol. Cytol.* 1988; 51: 1–34

Necker R, *J Comp Physiol A* **156**: 391-394 (1985).

Norberg, U, In Ecological morphology (PC Wainwright, SM Reilly, Eds.), The University of Chicago Press Ltd, London (1994).

Norberg UM, Rayner JM, *Philos Trans R Soc Lond B Biol Sci* **316**: 335-427 (1987).

Olshausen BA, Field DJ, *Curr. Opin. Neurobiol.* 2004;14: 481–487

Pei YC, *et al., J Neurophysiol* **102**:1843-53 (2009).

Pflüger HJ, Tautz J, *J Comp Physiol* **145** 369–80 (1982).

Poncharal P, *et al.*, *Science* **289** 1513–6 (1999).

Quay WB, *Anat. Rec.* 1970; 166: 189–197

Quist BW, *et al.*, *Biomech* **44**: 2775–81 (2011).

Riskin DK, et al., *J. Theor. Biol.* 2008; 254: 604–615

Rutlin M, *et al.*, *Cell* **159**:1640-51 (2014).

Ryan JM, et al., *Acta Anat. (Basel)*. 1997; 158: 121–129

Sakurai K, *et al.*, *Cell Reports* **5**:87-98 (2013).

Sane SP*, et al.*, *Science* **315** 863–6 (2007).

Shimozawa T, Kanou M, J *Comp Physiol* A **155**,495 -505 (1984).

Shimozawa T, *et al.,* In *Sensors and Sensing in Biology and Engineering* (ed. FG Barth, JAC Humphrey, T Secomb), pp. 145-157, Springer (2003).

Simmons JA, et al. *Science*. 1979; 203: 16–21

Smola U., *Z Vergl Physiol* **70**: 335–348 (1970).

Sterbing-D'Angelo SJ, *et al.*, *Proc Natl Acad Sci USA* **108**, 11291 (2011).

Sterbing-D'Angelo SJ, *et al.*, *Bioinspir Biomim* **11** 056008 (2016).

Sterbing-D'Angelo, *et al.*, *J Neurophysiol*, pp.jn-00261 (2017, epub ahead of print).

Swanson GJ, Lewis J, *J. Embryol. Exp. Morphol.*1986; 95: 37–52

Swartz SM, et al., *J. Zool.* 1996; 239: 357–378

Szwed M, et al., *Neuron*. 2003; 40: 621–630

Takahashi Y, Nakajima Y, *Pain*. 1996; 67: 197–202

Takahashi Y, et al., *J. Comp. Neurol.* 2003; 462: 29–41

Taylor GK, Krapp HG, *Adv Insect Physiol* **34**: 231-316 (2007).

Thewissen JG, Babcock SK, *Science*. 1991; 251: 934–936

Tokita M, et al. *Nat. Commun.* 2012; 3: 1302

Vickery RM, *et al. J Physiol* **474**:379 (1994).

Wang G, Scott SA, *Dev. Biol.* 2002; 251: 424–433.

Weatherbee SD, *et al., Proc Natl Acad Sci* **103**:15103–15107 (2006).

Williams CM, Kramer EM. ,*PLoS ONE* 5, e8806 (2010).

Witney AG, et al. *Trends Neurosci.* 2004; 27: 637–643

Woodbury CJ, Koerber HR, *J. Comp. Neurol.* 2007; 505: 547–561

Xu J, Wall JT, *J. Comp. Neurol.* 1999; 411: 369–389.

Yin J, et al., *Sci. China C. Life Sci.* 2009;52: 802–806

Yu YSW, *et al.,* J *Exp Biol* **219** 937–48 (2016).

Zook JM, Fowler BC, *Myotis* **23-24**:31-36 (1986).

Zook JM. In: *Evolution of Nervous Systems*. Vol. 3, ed Kaas JH, Academic Press, Oxford, pp. 215-226 (2006).